https://doi.org/10.5194/wes-2025-217
Preprint. Discussion started: 30 October 2025

eawe european academy of wind energy
Open Access WIND ENERGY SCIENCE DISCUSSIONS

Flow Field Analysis of a Leading-Edge Inflatable Kite Rigid Scale Model Using Stereoscopic Particle Image Velocimetry

Jelle Agatho Wilhelm Poland[1], Erik Fritz[1,2], and Roland Schmehl[1]

[1]Faculty of Aerospace Engineering, Delft University of Technology, Kluyverweg 1, 2629 HS, Delft
[1]TNO, Kessler Park 1, 2288 GS Rijswijk, The Netherlands

Correspondence: Jelle Agatho Wilhelm Poland (j.a.w.poland@tudelft.nl)

Abstract. Leading-edge inflatable (LEI) kites are characterized by a pronounced downward curvature of the wing and flow recirculation zones on the pressure side. This study presents novel stereoscopic particle image velocimetry (PIV) measurements of a 1:6.5 rigid scale model of the TU Delft V3 LEI kite. The flow-field measurements were conducted in the Open Jet Facility of Delft University of Technology for two angles of attack and seven chordwise measurement planes positioned between mid-span and tip, and were compared with results from Reynolds-averaged Navier–Stokes (RANS) simulations. The double-curved anhedral wing geometry presented several challenges, such as surface reflections that required careful data processing and the use of a lateral velocity filter. The circulation distribution was analyzed, using both elliptical and rectangular boundary curves, showing good agreement in trends between the vortex-step method (VSM), RANS, and PIV data. The lift and drag coefficients of each chordwise measurement plane were estimated using the Kutta–Joukowski theorem, surface pressure integration of RANS CFD data, and Noca's method—an inherently three-dimensional reformulation of the momentum conservation equations expressed solely as surface integrals over the control-volume boundary—applied here in two dimensions. While the mid-span to tip variation of lift coefficients was in accordance with the anhedral shape and tip-vortex effects, the drag measurements and predictions deviated from the expected behavior by exhibiting negative values. Especially near the tip region, significant discrepancies were observed, attributed to increased measurement uncertainty. The surface pressure integration revealed discrepancies at the strut junction, likely due to local three-dimensional strut-induced flow effects and increased airfoil thickness. This study provides comprehensive validation data for CFD simulations of LEI kites while highlighting the challenges in PIV measurements of double-curved anhedral wings and characterizing local aerodynamic phenomena.

1 Introduction

Leading-edge inflatable (LEI) kites are used for kite-surfing and novel renewable energy applications such as wind-assisted ship propulsion and airborne wind energy. This specific type of kite uses an inflated tubular frame to collect the aerodynamic load generated by a canopy and transmit this via a system of bridle lines to one or more tethers. Their design as a single morphing aerodynamic control surface makes LEI kites highly maneuverable, which is a crucial requirement for the mentioned applications (Breukels, 2011). Pitch control is achieved by symmetric actuation of the bridle line system (Hummel et al., 2019), directional control by asymmetric actuation (Elfert et al., 2024). The wings are generally downward curved to minimize the

https://doi.org/10.5194/wes-2025-217
Preprint. Discussion started: 30 October 2025

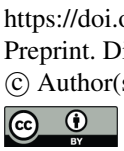

eawe european academy of wind energy
Open Access WIND ENERGY SCIENCE DISCUSSIONS

spanwise stresses in the bridled membrane structure. While the vertical wing area contributes to the favorable yaw authority, the sweep of the wing extends the depower range of the kite. In addition to the actuation-induced morphing, the shape of the membrane wing is also subject to aero-structural coupling effects. The kite investigated in the present study is illustrated in Fig. 1 and described in more detail in Oehler and Schmehl (2019).

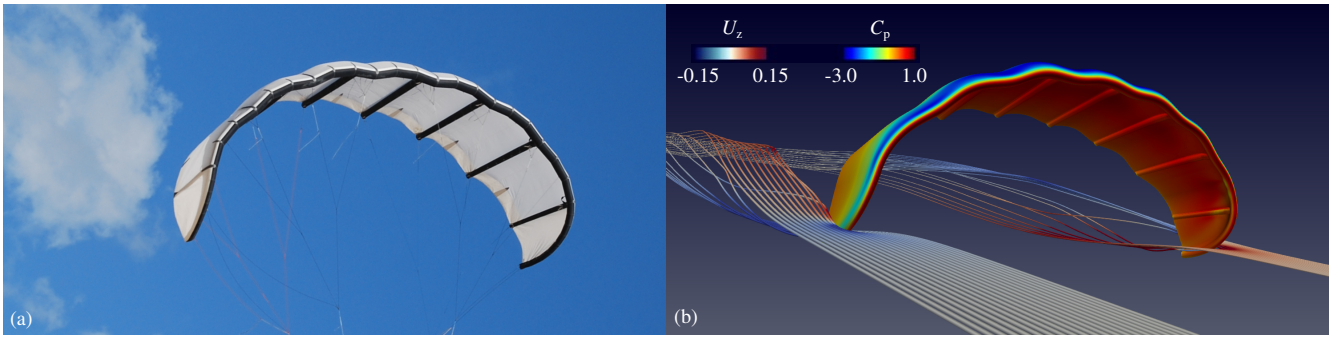

Figure 1. TU Delft V3 kite designed for airborne wind energy harvesting: (a) 2012 prototype with a flat wing surface area of 25 m^2; (b) CFD visualization of the flow around the design geometry, depicting the non-dimensional surface pressure C_p on the wing and the flow velocity z-component U_z coloring streamlines along the flow around the wing tips (adapted from Viré et al., 2022).

Characterizing the aerodynamics of LEI kites with numerical prediction and experimental measurement poses several challenges, owing to the highly flexible nature, pronounced anhedral and sweep, and unconventional airfoil geometries. For example, the backward-facing step formed by the inflated leading-edge tube and attached single-skin canopy leads to flow separation and recirculation zones on the wing's pressure side, already at low angles of attack. Consequently, fast potential flow solvers can not be used to analyze the two-dimensional (2D) aerodynamics (Poland et al., 2025a). Instead, computational fluid dynamics (CFD) solvers based on Reynolds-averaged Navier–Stokes (RANS) equations have to be employed, substantially increasing the computational resource demands for early design iterations (Folkersma et al., 2019). To avoid this computational overhead, which can become excessive when the wing geometry changes continuously, Breukels (2011) derived polynomial approximations of the aerodynamic coefficients C_L, C_D, and C_M from CFD simulations of a large variety of parametrized LEI airfoil shapes. Subsequent studies refined the airfoil parametrization and used machine learning to develop regression models with a wider parametric range (Watchorn, 2023; Masure, 2025). To expand the 2D aerodynamic properties to three-dimensional (3D) wings, lifting-line methods (Gaunaa et al., 2011; Leloup et al., 2013) and vortex-step methods (VSM) (Damiani et al., 2019; Cayon et al., 2023) have been used successfully. Especially the implementation of pre-computed, shape-dependent airfoil aerodynamic coefficients in the VSM framework proves to deliver high-quality results (Poland et al., 2025a). RANS simulations of complete LEI kites have also been conducted, with parametric sweeps in Reynolds number, angle of attack and sideslip angle, indicating that the strut tubes exert a negligible influence on the integral aerodynamic properties (Viré et al., 2020, 2022).

Experimental analyses of kite aerodynamics are generally most reliable when conducted in a wind tunnel under controlled flow conditions (De Wachter, 2008; Desai et al., 2024). However, industrial-scale kites in the size range of 50 to 500 m^2 can not be mounted at full scale in wind tunnel facilities. On the other hand, reverting to scale models requires preserving aeroelastic

https://doi.org/10.5194/wes-2025-217
Preprint. Discussion started: 30 October 2025

eawe european academy of wind energy
Open Access WIND ENERGY SCIENCE DISCUSSIONS

similarity, which is challenging for a bridled inflatable membrane structure. A practical option is to decrease the complexity of the fluid-structure interaction problem by investigating the aerodynamics of a rigid scale model, such as presented by Belloc (2015) for a reference paraglider wing. A similar approach was pursued by Poland et al. (2025b), measuring the aerodynamic loads on a rigid scale model of the TU Delft V3 kite for different angles of attack, sideslip angles, and Reynolds numbers. The measured forces and moments corroborate numerical predictions from CFD and VSM simulations within the nominal operating regime, encompassing angles of attack from $2°$ to $8°$ and sideslip angles of $\pm 10°$, as reported by Cayon et al. (2025).

Although numerical studies have significantly advanced the understanding of LEI airfoil aerodynamics and integral effects of the airfoil loading, a detailed experimental analysis of the flow around this specific type of wing has not been reported in the literature. Particle image velocimetry (PIV) offers a non-intrusive method to capture planar flow fields, with minimal influence from introduced tracer particles. Stereoscopic PIV, employing two cameras, mitigates potential errors caused by perspective distortions in velocity measurements (Prasad, 2000). The resulting flow fields enable evaluation of local 2D aerodynamic properties, including circulation, induction, inflow angles, forces, and aerodynamic coefficients (Fritz et al., 2024a). Circulation can be determined by defining a boundary curve and interpolating velocity components along it. Forces may subsequently be estimated on this boundary using Noca's method (Noca et al., 1999).

The present paper describes a novel stereoscopic PIV analysis of a rigid scale model of the TU Delft V3 LEI kite with the goal of obtaining spatially resolved flow-field data. The data was acquired in seven chordwise measurement planes along the wing span, for two angles of attack. Sources of uncertainty were systematically assessed, local strut effects were investigated, and a novel masking approach accompanied by a detailed sensitivity analysis was introduced. The resulting flow fields were used to calculate local aerodynamic properties, such as circulation and sectional aerodynamic coefficients. The primary outcome is an investigation of underlying aerodynamic phenomena through comparison of experimentally measured and numerically simulated flow fields, conducted qualitatively and quantitatively, the latter based on circulation and 2D force estimates.

The remainder of the paper is organized as follows. Section 2 describes the experimental methodology, including the wind tunnel, rigid scale model, experimental setup, stereoscopic PIV technique, test cases, data processing, and methods for deriving aerodynamic quantities. Section 3 presents the results, including uncertainty analysis, qualitative comparisons between CFD and PIV, and quantitative comparisons. A discussion of the results follows in Sect. 4, addressing PIV measurement limitations, an analysis of quantitative discrepancies, and local strut effects. Conclusions and recommendations for future research are presented in Sect. 5.

2 Method

This section outlines the specifications of the wind tunnel, the scale model, the experimental setup, and the PIV technique. The arrangement of the measurement planes is discussed next, followed by the data processing steps, and a description of how integral aerodynamic quantities are derived from planar flow field data.

https://doi.org/10.5194/wes-2025-217
Preprint. Discussion started: 30 October 2025

eawe european academy of wind energy
Open Access WIND ENERGY SCIENCE DISCUSSIONS

2.1 Wind tunnel

The wind tunnel experiments were conducted in the closed-loop Open Jet Facility (OJF) of the TU Delft from 8 to 12 April 2024. The tunnel has an octagonal exhaust nozzle measuring 2.85×2.85 m and is equipped with a 500 kW electric motor and a large fan generating a flow speed up to 35 ms^{-1}. To ensure uniform flow conditions in the test section, the tunnel uses corner guide vanes and wire meshes. The maximum reported turbulence intensity in the test section is 0.5% (Lignarolo et al., 2014). While the load measurements in (Poland et al., 2025b) were done for several wind speeds, the PIV measurements used a fixed wind speed of $U_\infty = 15$ ms^{-1}, with variations from the set point up to 0.2%. The inflow and atmospheric conditions for each measurement were logged to later be able to correctly non-dimensionalize the data, which was particularly important in this campaign as the temperature ranged from 22 to 32 °C due to a malfunctioning cooling system. Wind tunnel corrections were needed and applied to the angle of attack to account for blockage effects (Poland et al., 2025b).

2.2 Rigid scale kite model

To manufacture a rigid scale model of the V3 kite, the wing geometry adapted for the CFD simulations by Viré et al. (2022) was used, as detailed in the companion paper (Poland et al., 2025b). This CFD geometry differed slightly from the original design: the bridle line system was omitted, the trailing edge connecting the upper and lower wing surfaces was rounded, and edge fillets were applied to all tubular frame–to–canopy connections. Using the CFD geometry was motivated by the measurement data's intended purpose for validating computational studies. The wing was scaled down by a factor of 1:6.5, resulting in the dimensions outlined in Table 1, and the Reynolds number

$$\mathrm{Re} = \frac{\rho U_\infty c_{\mathrm{ref}}}{\mu} = 3.8 \times 10^5, \tag{1}$$

where $\rho = 1.2$ kgm^{-3} denotes the density, $U_\infty = 15$ ms^{-1} the inflow speed, $c_{\mathrm{ref}} = 0.396$ m the reference chord, and $\mu = 1.89 \times 10^{-5}$ the dynamic viscosity. The scale model mounted in the test section is shown in Fig. 2.

Table 1. Dimensions of the 1:6.5 scale model. Chord length, height, and width of the manufactured model deviate by no more than 1 mm from the scaled geometry, as verified using a laser tracker (Poland et al., 2025b).

Property	Symbol	Value	Unit
Mid-span chord	c_{ref}	0.396	m
Height	h	0.462	m
Width	W	1.278	m
Mass	m	7.965	kg
Flat surface area	S	0.59	m^2
Planform area	A	0.46	m^2
Projected frontal area at $\alpha = 24°$	A_{f}	0.2	m^2

https://doi.org/10.5194/wes-2025-217
Preprint. Discussion started: 30 October 2025

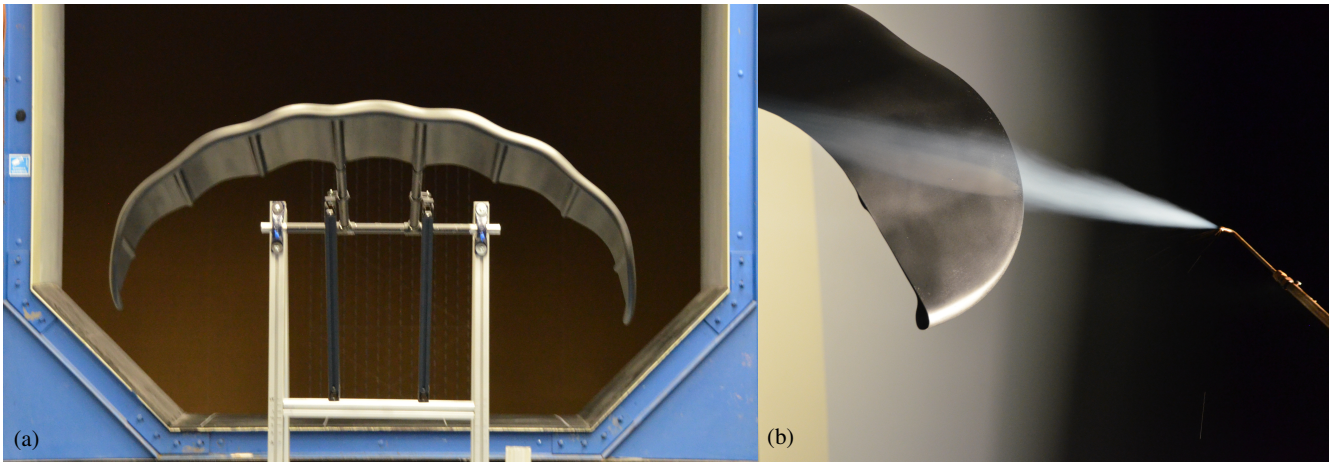

Figure 2. Wind tunnel setup: (a) Rigid scale model in the wind tunnel, swiveled by 180 ° with its back facing the octagonal OJF exhaust nozzle; (b) Smoke trail visualisation of the flow over a wing tip.

2.3 Experimental setup

The scale model is positioned in the center of the octagonal jet-exhaust using a support structure of aluminum beams. Two steel rods extend from the wing's center struts and connect the scale model to the support frame, as shown in Fig. 2(a) and detailed in the companion paper (Poland et al., 2025b). The images in Fig. 3 depict the normal and upside-down configurations, respectively, for analyzing the flow field on both sides of the wing with the cameras positioned on the ground. The highlighted horizontal bar was used to adjust the angle of attack α of the wing, achieving an accuracy of $0.1°$ as measured by digital inclinometers. Both the cameras and the laser were mounted on a motorized traverse system with a step size of 0.01 mm in the x and y directions. This configuration permitted measurements at multiple chordwise and transverse (y) locations without the need to refocus the cameras or recalibrate the software. Due to the wing's downward curvature, the distance between the PIV system and the measurement plane varied. To ensure the wing remained within the camera field of view, its vertical position was adjusted for certain measurements by raising the blue table supporting the structure, as shown in Fig. 3.

2.4 Stereoscopic particle image velocimetry

The flow field around the wing was measured non-intrusively with stereoscopic particle image velocimetry (PIV). The flow, seeded with tracer particles, was captured by two synchronised cameras, each recording pairs of images with a time delay of 100 µs. The flow field was determined by comparing these sets and tracking the displacement of particle groups. Laser control, camera synchronization, and image acquisition were all triggered by a single pulse signal from an opto-coupler (TCST 2103), controlled via LaVision's DaVis 8 software. For each plane, each camera recorded a total of 250 image sets at 15 Hz, which, as demonstrated in Fig. D1 in Appendix D, was sufficient to ensure statistical convergence for time-averaged results.

https://doi.org/10.5194/wes-2025-217
Preprint. Discussion started: 30 October 2025

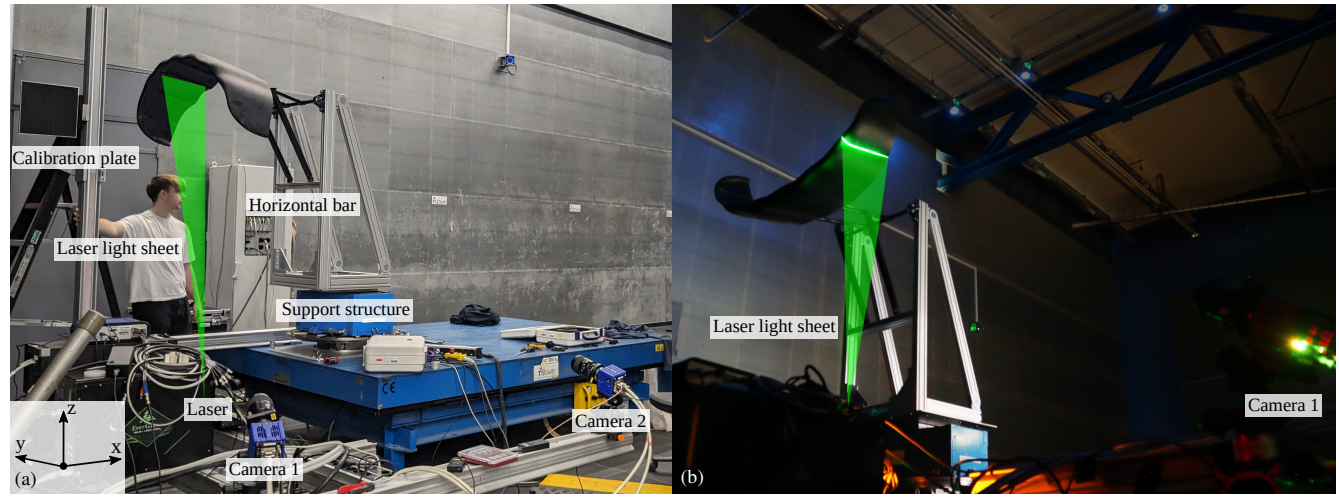

Figure 3. Experimental setup: (a) Photograph showing the labelled components of the setup and the axis orientations; (b) Long-exposure photo of the laser light sheet projected onto the model. In this instance, the laser light sheet spans the entire chord, a coverage not typical during standard measurements, achieved here by operating the system in laser alignment mode. In both photos, the laser light sheet was graphically enhanced.

A Quantel Evergreen double-pulsed neodymium-doped yttrium aluminum garnet laser was used as the light source, with a wavelength λ_{L} of $532\ \mathrm{nm}$, shaped into an approximately $3\ \mathrm{mm}$ thick laser light sheet. As illustrated in Fig. 3, the generated vertical sheet illuminates a flow-aligned cross-section of the floor-facing side of the wing. To reduce light reflections, both the wing and relevant parts of the support structure were spray-painted matte black. A Safex smoke generator produced tracer particles with a median diameter of $1\ \mu\mathrm{m}$. The generator was positioned downstream of the tunnel test section to ensure a homogeneous mixing of the particles with the flow before re-entering the test section.

The two LaVision Imager sCMOS cameras, with an f-number $f_{\#} = 8$, defined as the ratio between focal length and aperture diameter (Raffel et al., 2018), were placed at radial distances of 1.70 and $1.95\ \mathrm{m}$ from the laser light sheet. This configuration resulted in a field of view (FOV) of $0.42 \times 0.36\ \mathrm{m}$. The cameras had a sensor resolution of 2560×2160, a pixel size $p_{\mathrm{size}} = 6.5$ $\mu\mathrm{m}$ corresponding to a spatial sampling density of 6.41 pixels per millimeter. The magnification factor M, defined as the image size divided by the object size, was computed along the x-axis. A sensor width of $2160\ \mathrm{px}$ with a pixel size of $6.5\ \mu\mathrm{m}$, over a $0.36\ \mathrm{m}$-wide field of view, resulted in a value of $M = 0.039$. The ratio of the diffraction diameter of the particles to the pixel diameter is recommended to be higher than one to minimize peak locking errors (Raffel et al., 2018; Bensason et al., 2025). It was calculated using

$$\frac{d_{\mathrm{diff}}}{p_{\mathrm{size}}} = \frac{2.44 f_{\#}(M+1)\lambda_L}{p_{\mathrm{size}}} = 1.7. \tag{2}$$

The cameras were calibrated using a target with a known grid pattern, visible as a black square on the left side of Fig. 3(a). The calibration was verified by comparing the measured distances between reference points with their known physical spacing.

https://doi.org/10.5194/wes-2025-217
Preprint. Discussion started: 30 October 2025

eawe european academy of wind energy
Open Access WIND ENERGY SCIENCE DISCUSSIONS

2.5 Test cases

Because the scale model is symmetric with respect to the center chord and only symmetric inflow conditions were considered, the measurements were limited to one half of the wing. Seven measurement planes denoted as $Y1$ through $Y7$ were selected, as shown in Fig. 4. To align with available CFD simulation results, the measurements were conducted at angles of attack $\alpha = 7$ and $17°$, with the larger value also covering stall phenomena (Poland et al., 2025a).

The positions of the bottom left corners of the measurement planes for the suction-side-up configuration, shown in Fig. 5, are listed in Table 2 and measured relative to the mid-span leading-edge point. The table height was kept fixed for $Y1$ through $Y4$, and ideally, the vertical position z at the top of each measurement plane would be zero. However, small offsets were observed and attributed to minor imperfections in the experimental setup. These offsets were corrected in the post-processing by aligning the raw image light intensity with the expected cross-section location. For each measurement plane, the images were iteratively shifted until a precise match was achieved.

As visible in Fig. 4, only the mid-span plane $Y1$ was perpendicular to the wing surface. Moving outwards from $Y1$ to $Y7$, the vertical planes became progressively more aligned with the wing surface as a result of its downward curvature. Toward the tip, this alignment caused the velocity component normal to the measurement plane to increase, which is more difficult to accurately capture (Prasad and Adrian, 1993; Prasad, 2000). Due to time constraints, the measurements at $\alpha = 17\ °$ were limited to $Y1$ through $Y4$.

2.6 Data processing

The measurements were processed using LaVision's DaVis 10 software (LaVision GmbH, 2025). The procedure consisted of the following steps: (1) averaging the image sequence; (2) normalizing each image by the computed average; (3) applying a temporal filter with a filter length of five images; (4) applying masks to exclude regions not of interest; (5) performing the PIV analysis using interrogation windows of 64×64 px^2 with two passes and 50% overlap; and (6) averaging the resulting vectors, including only data with at least 25 source vectors and falling within two standard deviations of the mean. The first and second steps normalize the local light intensity to enhance particle detection, which proved particularly useful in regions affected by reflections.

For each y location, six overlapping measurements were taken, as shown in Fig. 5. The data in the overlapping regions were stitched together to form a continuous flow field. The grid was evaluated sequentially along rows, corresponding to the x-direction. To ensure a smooth transition, data points from overlapping measurements were weighted based on their relative distance from the edges of the combined region. In the remainder of the paper, the result of stitching these six measurements is referred to as a single measurement plane.

2.7 Derivation of integral aerodynamic quantities

The PIV measurements yield 2D datasets of scalar- and vector-valued flow field properties, including the spatial coordinates $\mathbf{x}$, the streamwise, lateral, and vertical components u_x, u_y, and u_z, respectively, the velocity magnitude u, and the spatial

https://doi.org/10.5194/wes-2025-217
Preprint. Discussion started: 30 October 2025

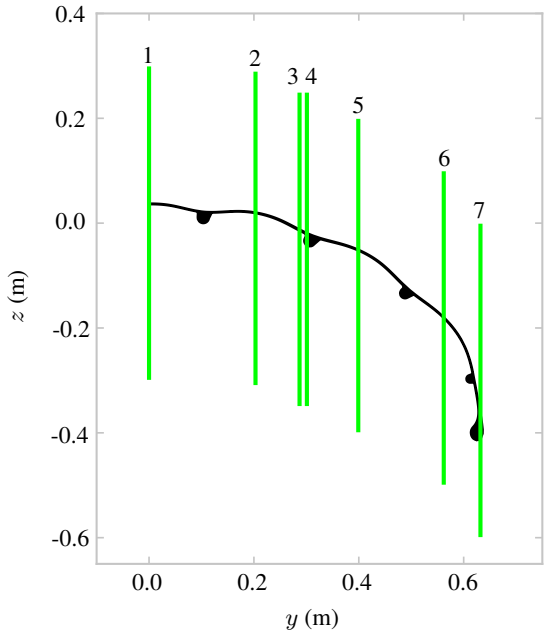

(a)

Figure 4. Arrangement of the measurement planes along the span, for $\alpha = 7°$ at 10% x/c aft of the mid-span leading edge.

Table 2. Reference positions of measurement planes, i.e., bottom left corners, see Fig. 5, at $\alpha = 0°$.

	x (m)	y (m)	$z_{\alpha=7}$ (m)	$z_{\alpha=17}$ (m)
$Y1$	0	0.000	-0.000	-0.000
$Y2$	0	0.203	-0.004	-0.000
$Y3$	0	0.287	-0.001	-0.001
$Y4$	0	0.301	-0.005	-0.006
$Y5$	0	0.399	-0.120	—
$Y6$	0	0.562	-0.111	—
$Y7$	0	0.632	-0.244	—

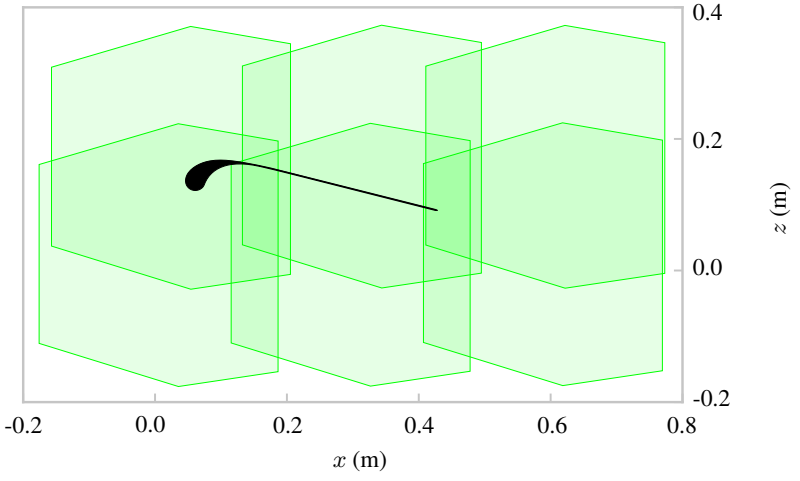

(a)

Figure 5. Mid-span cross-sectional view showing the LEI airfoil and the six overlapping measurement regions that together form plane $Y1$. The intentional overlap ensures full coverage of the flow field.

https://doi.org/10.5194/wes-2025-217
Preprint. Discussion started: 30 October 2025

eawe european academy of wind energy
Open Access WIND ENERGY SCIENCE DISCUSSIONS

derivatives of the velocity components. From this discrete data, the components u_x and u_z are interpolated along a suitable closed planar boundary curve S around the airfoil. This allows for the computation of the circulation Γ as a line integral of the velocity field

$$\Gamma = \oint_S \mathbf{u} \cdot \mathrm{d}\mathbf{s}, \tag{3}$$

quantifying the rotational strength of the flow in that region. Given the circulation, the 2D lift per unit span can be approximated using the Kutta–Joukowski theorem (Anderson, 2016)

$$C_{\mathrm{l'},\mathrm{Kutta}} = \frac{2\Gamma}{U_\infty c_{\mathrm{ref}}}. \tag{4}$$

This equation assumes that the integration boundary lies within the potential flow region surrounding the object of interest and that the flow is steady and attached. Nevertheless, although derived from an inviscid formulation, the circulation-based method retains theoretical validity in viscous flows, with Liu et al. (2015) proving the exact applicability of the Kutta–Joukowski relation under steady 2D viscous and compressible conditions. In the present context, these assumptions are only approximately satisfied, as the flow is incompressible and quasi-steady but locally 3D and measured in the near field, so that circulation-based estimates should be interpreted as approximate rather than exact.

An alternative approach for force estimation is based on integrating the momentum change over a finite control volume. However, when using PIV measurements, reflections from the object surface often prevent reliable data acquisition near the body. Noca et al. (1999) proposed an alternative formulation of the momentum conservation equations that relies solely on surface integrals of flow quantities evaluated along the boundary of the control volume. This approach facilitates force estimation from flow field measurements without requiring velocity data throughout the entire control volume. Noca's method has been successfully applied in such contexts to flow data from both horizontal-axis wind turbines (Fritz et al., 2024a, b) and vertical-axis wind turbines (LeBlanc and Ferreira, 2022). The method, expressed in symbolic notation, evaluates the force per unit density as,

$$\frac{\mathbf{F}}{\rho} = \oint_S \mathbf{n} \cdot \boldsymbol{\gamma}_{\mathrm{flux}} \mathrm{d}s - \oint_{S_\mathrm{b}} \mathbf{n} \cdot (\mathbf{u} - \mathbf{u}_\mathrm{b})\, \mathbf{u} \mathrm{d}s - \frac{d}{dt} \oint_{S_\mathrm{b}} \mathbf{n} \cdot (\mathbf{u}\mathbf{x})\, \mathrm{d}s, \tag{5}$$

where

$$\begin{aligned}\boldsymbol{\gamma}_{\mathrm{flux}} =& \frac{1}{2}u^2\mathbf{I} - \mathbf{u}\mathbf{u} - \frac{1}{\mathscr{N}-1}\mathbf{u}(\mathbf{x}\times\boldsymbol{\omega}) + \frac{1}{\mathscr{N}-1}\boldsymbol{\omega}(\mathbf{x}\times\mathbf{u}) \\ & - \frac{1}{\mathscr{N}-1}\left(\mathbf{x}\cdot\frac{\partial\mathbf{u}}{\partial t}\right)\mathbf{I} + \frac{1}{\mathscr{N}-1}\mathbf{x}\frac{\partial\mathbf{u}}{\partial t} - \frac{\partial\mathbf{u}}{\partial t}\mathbf{x} \\ & + \frac{1}{\mathscr{N}-1}[\mathbf{x}\cdot(\boldsymbol{\nabla}\cdot\boldsymbol{\tau})]\mathbf{I} - \frac{1}{\mathscr{N}-1}\mathbf{x}(\boldsymbol{\nabla}\cdot\boldsymbol{\tau}) + \boldsymbol{\tau},\end{aligned} \tag{6}$$

and $\mathbf{n}$ is the normal vector on the bounding curve, S is the outer boundary curve of the control volume surrounding the immersed body, S_b is the inner boundary curve prescribed by the immersed body's surface, $\mathbf{u}_\mathrm{b}$ is the velocity vector of the immersed body's surface, $\mathscr{N}$ represents the number of dimensions, $\boldsymbol{\omega}$ the angular velocity vector of the immersed body, $\mathbf{x}$ is

https://doi.org/10.5194/wes-2025-217
Preprint. Discussion started: 30 October 2025

eawe european academy of wind energy
Open Access WIND ENERGY SCIENCE DISCUSSIONS

the position vector, $\mathbf{I}$ the identity tensor, and $\boldsymbol{\tau}$ the viscous stress tensor. The second term on the right-hand side of Eq. (5) represents the momentum flux through the body surface. Because the scale model has a solid, impermeable surface, this contribution vanishes. The third term is also zero, as it accounts for forces due to boundary acceleration. In the present case, the scale model is assumed to remain stationary, and, because the no-throughflow condition on the body surface, $\mathbf{n} \cdot \mathbf{u} = 0$, also enforces the product $\mathbf{n} \cdot (\mathbf{ux})$ to vanish.

Equation (6) describes ten individual contributions: the first four, presented in the first line, are inviscid contributions, the following three are time-dependent and are zero for steady flow. The final three contributions account for viscous effects. While Noca's method is inherently 3D, it is here applied to a pseudo 2D incompressible flow problem by setting the out-of-plane velocity u_y to zero. Other out-of-plane quantities, such as the vorticity component ω_y, are retained, consistent with the pseudo 2D flow assumption. This simplification reduces the expression accordingly, see App. A for the full derivation. The resulting 2D method facilitates the calculation of normal and tangential force components from a defined boundary path in a flow field.

Since the CFD simulations provide the flow field for the entire domain, 2D aerodynamic forces can also be derived via surface pressure and surface shear force integration. The total aerodynamic force acting on the airfoil is computed as

$$\mathbf{F} = \rho \oint_{S_\mathrm{b}} \mathbf{n} \cdot (-p\mathbf{I} + \boldsymbol{\tau}) \, \mathrm{d}s, \tag{7}$$

where p represents the static pressure.

3 Results

This section presents the results obtained from stereoscopic PIV experiments, including an uncertainty assessment, a qualitative comparison of measured and simulated velocity fields, and a quantitative analysis of circulation and aerodynamic loads. Masking procedures were necessary due to surface reflections. The details are provided in App. B.

3.1 Uncertainty analysis

The uncertainty in velocity measurements for time-averaged analyses can be expressed using the standard uncertainty $\mathrm{u}_{\bar{\mathrm{u}}}$ (Sciacchitano and Wieneke, 2016; Huang et al., 2023; Bensason et al., 2025),

$$\mathrm{u}_{\bar{\mathrm{u}}} = k \frac{\sigma_\mathrm{u}}{\sqrt{N}}, \tag{8}$$

where N is the number of images, and $k = 1.96$ denotes the coverage factor corresponding to a 95% confidence interval. Average velocity uncertainties are summarized in Table 3. The data indicate that uncertainties increase toward the wingtip, which is consistent with greater measurement-plane misalignment and enhanced surface reflections. At an angle of attack of $\alpha = 17°$, where stall was anticipated from integral load measurements (Poland et al., 2025b), uncertainties are significantly higher. These observed trends should be taken into account when interpreting the subsequent qualitative and quantitative analyses.

https://doi.org/10.5194/wes-2025-217
Preprint. Discussion started: 30 October 2025

eawe european academy of wind energy
Open Access WIND ENERGY SCIENCE DISCUSSIONS

Table 3. Velocity standard uncertainties, corresponding to a 95% confidence interval, were calculated based on 250 images and all data points within a single measurement plane.

	$\alpha = 7°$							$\alpha = 17°$			
	$Y1$	$Y2$	$Y3$	$Y4$	$Y5$	$Y6$	$Y7$	$Y1$	$Y2$	$Y3$	$Y4$
$u_{\bar{u},x}$ $(-)$	0.03	0.04	0.04	0.04	0.04	0.05	0.05	0.11	0.12	0.11	0.13
$u_{\bar{u},y}$ $(-)$	0.06	0.07	0.07	0.07	0.08	0.07	0.08	0.14	0.19	0.19	0.22
$u_{\bar{u},z}$ $(-)$	0.06	0.07	0.07	0.07	0.09	0.08	0.09	0.13	0.21	0.21	0.25
$u_{\overline{u}}$ $(-)$	0.07	0.08	0.08	0.08	0.09	0.09	0.10	0.18	0.23	0.22	0.26

3.2 Qualitative comparison

The measured velocity fields are compared qualitatively against corresponding slices from CFD simulations by Viré et al. (2022), extracted at the same locations. The CFD results presented here have been corrected for a $1.02°$ offset in angle of attack, defined as the angle between the mid-span chord line and the apparent wind vector (Poland et al., 2025b). Velocity magnitude fields for the measurement planes are shown in Fig. 6 for sections $Y1$, $Y3$, and $Y4$ at $\alpha = 7°$, and for $Y1$ at $\alpha = 17°$. CFD results, available only at a $\mathrm{Re} = 10 \times 10^5$, are compared against measurements conducted at 3.8×10^5 under the assumption that Reynolds number differences are negligible. This assumption is supported by previous analysis of integral 3D forces and moments, which demonstrated convergence for increasing Re from 1.3×10^5 to 5×10^5 using the same experimental setup, model, and wind tunnel (Poland et al., 2025b). When examining the pressure side, notable discrepancies between the CFD and PIV velocity fields are observed. Both datasets capture the anticipated separation zone downstream of the leading-edge tube; however, the PIV measurements indicate a comparatively larger region of reduced velocity, shown as dark blue areas adjacent to the airfoil surface in Fig. 6. These lower-velocity regions occasionally extend several chord lengths from the airfoil, an effect absent in the numerical predictions. A similar discrepancy is observed on the suction side, particularly at measurement planes $Y3$ and $Y4$ for $\alpha = 7°$, where the PIV data exhibit reduced velocity magnitudes in regions where the simulations predict peak velocities associated with the suction-side low-pressure region. These anomalous low-velocity regions in the PIV data, inconsistent with CFD results and aerodynamic expectations, are attributed primarily to persistent surface reflections that were not fully mitigated by the u_y-component masking approach. Although these unresolved regions complicate the qualitative comparison, their impact on the quantitative analysis is minimal, as the selected integration boundary curves typically avoid intersecting such problematic areas.

Away from the airfoil surface, the qualitative comparison improves significantly, with both PIV and CFD velocity fields showing consistent magnitudes, e.g., in the wake region downstream of the wing. At $\alpha = 17°$, both the measurements and simulations consistently capture key flow features, including suction-side flow separation, a reduced velocity increase on the suction side, shear layer development, and the associated velocity gradients across this layer—indicating overall agreement in regions minimally affected by surface reflections. The suction-side flow regions confirm the anticipated stall regions from analysis of the 3D integral forces (Poland et al., 2025a).

https://doi.org/10.5194/wes-2025-217
Preprint. Discussion started: 30 October 2025

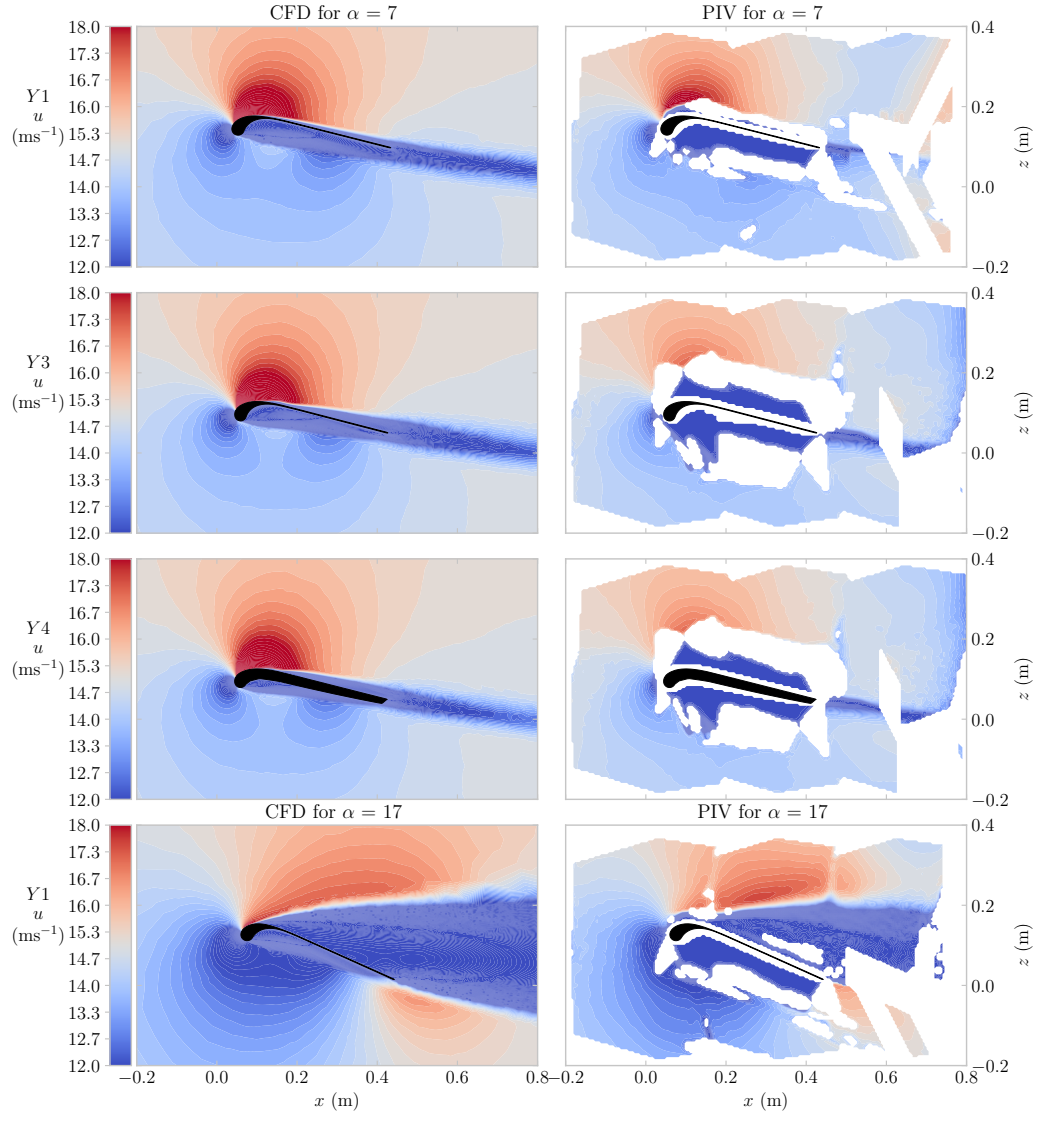

Figure 6. Comparing CFD-predicted to PIV-measured flow fields. The first column shows the computed velocity magnitude u at the exact locations, as the PIV measured results are shown in the second column. The rows in order are the results of $Y1$, $Y3$ and $Y4$ with α is 7° and $Y1$ with α is 17°.

https://doi.org/10.5194/wes-2025-217
Preprint. Discussion started: 30 October 2025

eawe european academy of wind energy
Open Access WIND ENERGY SCIENCE DISCUSSIONS

3.3 Quantitative results

Aerodynamic properties were computed by integrating flow field data along parameterized boundary curves. Two curve geometries—elliptical and rectangular—were assessed, as illustrated in Fig. 7. Each boundary curve is defined by a center position, rotation angle, width, height, and a specified number of boundary nodes. In cases where a boundary curve intersected regions lacking data, local interpolation of the flow field was performed prior to interpolating values onto the boundary nodes. A convergence study on lift and circulation, detailed in App. C, was conducted to determine appropriate boundary definitions; the final settings are summarized in Table 4. While CFD results demonstrated consistent convergence across boundary variations, PIV-derived quantities showed greater sensitivity. To reduce variability, circulation values from PIV were averaged over 100 slightly perturbed boundary sizes for each curve shape.

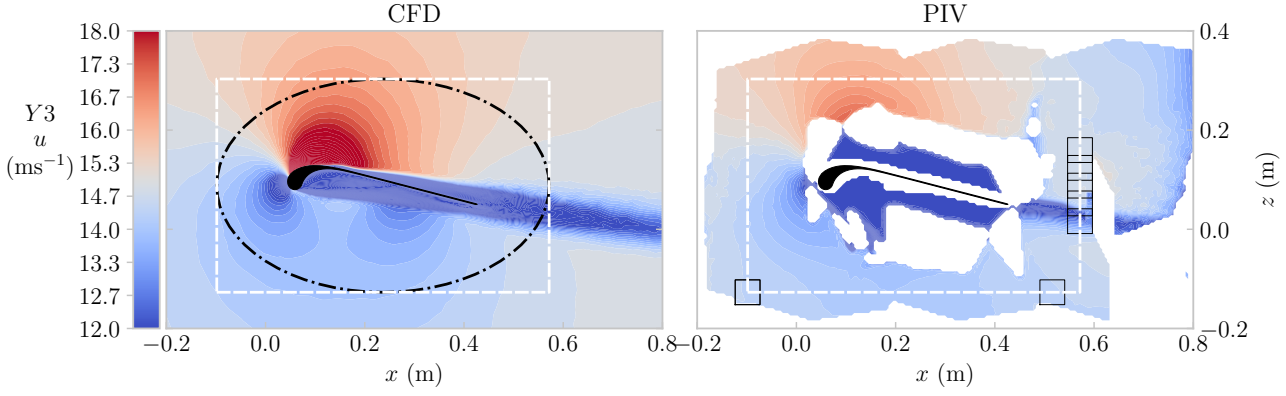

Figure 7. The velocity magnitude field, u, is shown for both CFD (left) and PIV (right) at plane $Y3$ and angle of attack $\alpha = 7°$. On the CFD plot, elliptical and rectangular bound curves are displayed, while the PIV plot features a rectangular bound curve along with interpolation squares.

The resulting circulation strength Γ distributions obtained from CFD and from PIV, which extend up to section $Y6$, are shown in Fig. 8. For reference, predictions from novel simulations using the vortex-step method (VSM) at a $\mathrm{Re} = 3.8 \times 10^5$ are also included, employing the recommended settings and 2D polars outlined in the companion paper (Poland et al., 2025a). Two distinct sources of uncertainty in the circulation measurements are represented by 90% confidence intervals (CIs). The first CI, shown as red-shaded areas, captures uncertainty due to velocity fluctuations across the 250 PIV images and is denoted as $\sigma_{\Gamma,\mathrm{u}}$. It is computed as the difference between the circulation derived from the mean velocity field and that obtained by perturbing the velocity field by one standard deviation. The second CI accounts for variations across the 100 different boundary shapes, denoted as $\sigma_{\Gamma,\mathrm{b}}$. Since these variations represent random approximations of the true circulation boundary, the corresponding standard deviation is scaled by $1/\sqrt{100}$ to reflect the averaging procedure. The total standard deviation σ_Γ,

https://doi.org/10.5194/wes-2025-217
Preprint. Discussion started: 30 October 2025

eawe european academy of wind energy
Open Access WIND ENERGY SCIENCE DISCUSSIONS

combining contributions from both velocity fluctuations and boundary shape variation, is computed as:

$$\sigma_\Gamma = \sqrt{\sigma_{\Gamma,\mathrm{u}}^2 + \sigma_{\Gamma,\mathrm{b}}^2}. \tag{9}$$

CFD-derived circulation distributions using elliptical and rectangular bound shapes were similar, though not identical; the influence of the bound shape diminished toward the wingtip, see Fig. 8. In contrast, PIV measurements were notably more sensitive: rectangular contours consistently yielded wider σ_Γ confidence intervals than elliptical ones, indicating greater uncertainty, primarily due to boundary-induced effects. The largest divergence occurred at $Y5$ ($y = 0.399$ m), where both the PIV contour discrepancy and the CFD–PIV mismatch peaked. Although RANS-based CFD and the Vortex-Step Method employ different numerical schemes, they predicted similar trends and magnitudes of circulation, verifying the correctness of the integration routine. Up to $Y3$, experimental and numerical circulations aligned-albeit less closely-providing additional validation. The overall agreement in distributed circulation indicates that the numerical tools accurately reproduce the distributed aerodynamic loads, and that the previously reported integral-lift agreement Poland et al. (2025a) was not a result of compensating errors.

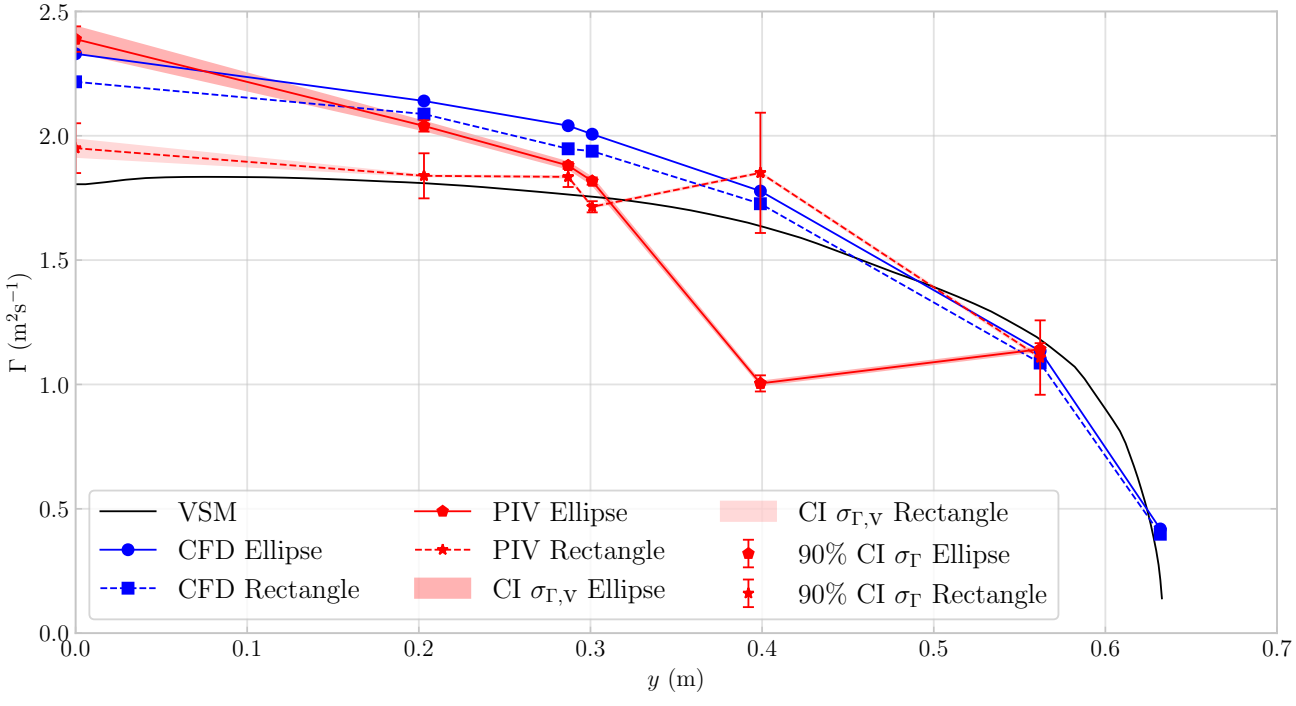

Figure 8. Circulation distribution at $\alpha = 7°$, computed using boundary curve velocity interpolation, is shown for CFD across all measurement planes, for PIV data up to plane $Y6$, and as predicted by the VSM method.

https://doi.org/10.5194/wes-2025-217
Preprint. Discussion started: 30 October 2025

eawe european academy of wind energy
Open Access WIND ENERGY SCIENCE DISCUSSIONS

The forces computed using the Kutta–Joukowski equation from circulation, the Noca's method, and pressure integration are summarized in Table 4 for both rectangular and elliptical boundary shapes. Only planes containing sufficient data for boundary curve interpolation are included in the analysis.

The Noca-derived values are consistent across both boundary shapes for CFD, whereas PIV results exhibit greater sensitivity to boundary shape, consistent with the circulation findings. Among the tested shapes, the ellipse provides the closest agreement between PIV and CFD, consistent with the smaller confidence intervals shown in Fig. 8. The CFD-derived $C_{\mathrm{l,\,Noca}}$ values at $Y3$ and $Y4$ are nearly identical, reflecting their close spatial proximity. At $Y1$, which has the lowest measurement uncertainty, the C_{l} values obtained using Noca's method are nearly identical for both CFD and PIV. Due to the presence of unphysical negative drag values on some planes, the $C_{\mathrm{d,\,Noca}}$ results are considered generally unreliable. Nonetheless, at $\alpha = 17°$, the elevated $C_{\mathrm{d,\,Noca}}$ values are consistent with anticipated and measured increases in 3D integral drag at the same angle of attack (Poland et al., 2025b).

The non-dimensional force calculated using the Kutta–Joukowski theorem, $C_{\mathrm{l,Kutta}}$, generally exhibits higher values than the reported lift coefficients. The differences between PIV and CFD results, as well as between elliptical and rectangular PIV boundaries, increased progressively towards the wingtip, consistent with previously noted effects of planar misalignment, reduced validity of the 2D assumption, and increasing out-of-plane flow, all contributing to elevated uncertainty. As shown in Fig. 8, the PIV ellipse result at $Y5$ deviates from the overall trend, which is reflected in the $C_{\mathrm{l,Kutta}}$ value, but not necessarily observed in $C_{\mathrm{l,Noca}}$ or $C_{\mathrm{d,Noca}}$.

The pressure integration values are comparable in magnitude to those obtained using Noca's method. However, from $Y1$ to $Y4$, the trend of decreasing aerodynamic performance predicted by Noca's method, the Kutta–Joukowski method, and VSM is not reflected in the pressure integration results. Notably, at $Y4$, both lift and drag increase. Possible causes for this discrepancy are examined in Sect. 4.

4 Discussion

This section interprets the experimental findings by addressing critical aspects of data quality and accuracy, followed by explanations for observed discrepancies between experimental and numerical results. The section first evaluates limitations inherent to the PIV measurements, subsequently discusses quantitative analysis discrepancies, and concludes with an investigation into local aerodynamic phenomena induced by the wing struts.

4.1 PIV measurement limitations

The raw PIV data showed anomalous regions, particularly near the airfoil surface on both suction and pressure sides. We hypothesize that these anomalies primarily result from surface reflections caused by the LEI wing's complex geometry, which includes a double-curved anhedral shape, a near-circular leading edge, and multiple strut elements. This explanation is supported by the increased occurrence of faulty regions in planes $Y3$ and $Y4$, both located near a strut, as shown in Fig. 6. Raw

https://doi.org/10.5194/wes-2025-217
Preprint. Discussion started: 30 October 2025

eawe european academy of wind energy
Open Access WIND ENERGY SCIENCE DISCUSSIONS

Table 4. Aerodynamic coefficients for the measured PIV and simulated CFD of different planes, using different calculation methods.

Plane	α	Boundary Setting			Ellipse		Rectangle			P-integration
					CFD	PIV	CFD	PIV		CFD
		x_b, z_b	0.24, 0.14 (m)	$C_{l,\,Noca}$ $(-)$	0.60	0.61	0.60	0.39	$C_{l,\,p}$ $(-)$	0.53
$Y1$	7°	W_b, H_b	0.6, 0.37 (m)	$C_{d,\,Noca}$ $(-)$	0.02	0.20	0.02	0.25	$C_{d,\,p}$ $(-)$	0.02
		N_b	360 $(-)$	$C_{l,Kutta}$ $(-)$	0.78	0.80	0.74	0.65		
		x_b, z_b	0.24, 0.12 (m)	$C_{l,\,Noca}$ $(-)$	0.57	0.43	0.57	0.36	$C_{l,\,p}$ $(-)$	0.49
$Y2$	7°	W_b, H_b	0.67, 0.39 (m)	$C_{d,\,Noca}$ $(-)$	-0.04	0.25	-0.05	0.35	$C_{d,\,p}$ $(-)$	0.02
		N_b	360 $(-)$	$C_{l,Kutta}$ $(-)$	0.72	0.68	0.70	0.62		
		x_b, z_b	0.24, 0.09 (m)	$C_{l,\,Noca}$ $(-)$	0.53	0.44	0.54	0.39	$C_{l,\,p}$ $(-)$	0.51
$Y3$	7°	W_b, H_b	0.67, 0.43 (m)	$C_{d,\,Noca}$ $(-)$	0.01	0.48	0.01	0.24	$C_{d,\,p}$ $(-)$	0.03
		N_b	360 $(-)$	$C_{l,Kutta}$ $(-)$	0.68	0.63	0.65	0.61		
		x_b, z_b	0.24, 0.09 (m)	$C_{l,\,Noca}$ $(-)$	0.53	0.51	0.54	0.36	$C_{l,\,p}$ $(-)$	0.73
$Y4$	7°	W_b, H_b	0.65, 0.42 (m)	$C_{d,\,Noca}$ $(-)$	-0.02	0.08	-0.02	0.16	$C_{d,\,p}$ $(-)$	0.08
		N_b	360 $(-)$	$C_{l,Kutta}$ $(-)$	0.67	0.61	0.65	0.57		
		x_b, z_b	0.23, 0.16 (m)	$C_{l,\,Noca}$ $(-)$	0.48	0.56	0.47	0.30	$C_{l,\,p}$ $(-)$	0.41
$Y5$	7°	W_b, H_b	0.70, 0.40 (m)	$C_{d,\,Noca}$ $(-)$	-0.08	-0.14	-0.08	-0.06	$C_{d,\,p}$ $(-)$	0.02
		N_b	360 $(-)$	$C_{l,Kutta}$ $(-)$	0.60	0.34	0.58	0.62		
		x_b, z_b	0.25, 0.09 (m)	$C_{l,\,Noca}$ $(-)$	0.57	0.77	0.58	0.77	$C_{l,\,p}$ $(-)$	0.41
$Y1$	17°	W_b, H_b	0.60, 0.44 (m)	$C_{d,\,Noca}$ $(-)$	0.29	-0.29	0.48	0.22	$C_{d,\,p}$ $(-)$	0.08
		N_b	360 $(-)$	$C_{l,Kutta}$ $(-)$	0.69	0.82	0.70	0.89		

image analysis further reveals a strong spatial correlation between these velocity anomalies and distinct geometric features, reinforcing the conclusion that surface reflections are the dominant source of error.

Despite various mitigation efforts, including support-structure masking, matte black spray paint, and dedicated post-processing, artifacts remained in the data. To mitigate their impact, a lateral velocity u_y filter was applied to exclude visibly faulty regions, as described in App. B. However, this filtering did not fully eliminate all anomalies, as indicated by the dark blue regions in Fig. 6. These areas were deemed faulty due to their clear mismatch with CFD results, which display smooth and physically consistent flow. Reflection-induced gaps in the data required interpolation near the surface, introducing localized uncertainties that reduce the fidelity of velocity gradients and derived aerodynamic quantities.

Measurements on both the suction and pressure sides were conducted on the same half of the wing, shown on the left in Fig. 2, thereby avoiding uncertainties related to geometric asymmetries. A randomized convergence study confirmed robust convergence of mean velocities over the 250-image sequence, see Fig. D1 in App. D.

Despite mitigation efforts, anomalous regions persisted and required interpolation, particularly near the airfoil surface, introducing localized uncertainties that reduce the fidelity of near-wall velocity gradients and, consequently, compromise the accuracy of aerodynamic force estimates.

https://doi.org/10.5194/wes-2025-217
Preprint. Discussion started: 30 October 2025

eawe european academy of wind energy
Open Access WIND ENERGY SCIENCE DISCUSSIONS

4.2 Quantitative analysis discrepancies

Incomplete velocity data near the airfoil surface necessitated interpolation to enable boundary curve analysis, inherently introducing uncertainty. This limitation is reflected in the sensitivity to boundary curve parameter selection, as demonstrated in App. C in Fig. C2. Averaging across a 10% parameter range reduced variability but did not fully eliminate it. Planes requiring minimal interpolation yielded the closest agreement in lift coefficient between PIV and CFD, see Table 4. In contrast, drag coefficients were less consistent and occasionally resulted in non-physical negative values.

In addition to interpolation-related effects, discrepancies may have also been introduced by the integration methods themselves. At $\alpha = 17°$, the 2D planar PIV-derived lift exceeded the CFD-predicted value—opposite to the trend observed in the 3D integrated force measurements reported in the companion paper (Poland et al., 2025b), where CFD produced higher lift. While this discrepancy likely reflects increased uncertainty at high angles of attack, it also suggests the presence of integration errors, as the trend was consistently observed in both Noca's- and Kutta–Joukowski-based force estimates.

To independently assess aerodynamic loads, surface pressure integration was conducted, incorporating both pressure forces F_{p} and viscous forces $F_{\mathrm{v,j}}$. Pressure forces dominated, with viscous contributions typically below 1%. Compared to values derived from boundary curves, see Table 4, the pressure integration results showed different magnitudes but similar trends, except at planes $Y3$ and $Y4$, where elevated lift and drag were observed. For $Y4$, the elevated values are partly attributed to the integration plane intersecting the strut section, which increases the effective airfoil thickness, shown in Fig. 6, thereby enhancing local camber. Supporting this interpretation is the observation that the discrepancy in trend is not captured by the bound integration methods. A further contribution could stem from a local strut effect, which, although smaller than at $Y4$, may also contribute to the off-trend increase in lift and drag observed at $Y3$.

4.3 Local strut effects

In the literature, CFD simulations have been performed both with struts (Viré et al., 2022) and without (Viré et al., 2020). Based on comparisons of global aerodynamic properties, it was concluded that the presence of struts has little influence on overall performance. However, Viré et al. (2022) noted that struts do affect the local flow field, including increased vortex shedding. This observation was supported by spanwise plots of the λ_2-criterion, which provides an indication of vortex core lines in (Jeong and Hussain, 1995). For the case $\alpha = 13°$ at a $\mathrm{Re} = 30 \times 10^5$, developing vorticity was found on the pressure side, with structures present between $x/c = 0.3$ and $x/c = 0.6$, except near the tip vortex and the strut regions—indicative of strut-induced effects. The work of Viré et al. (2022) is the published version of the MSc thesis by Lebesque (2020), which further reported that strut blockage influenced the location and size of recirculation regions and, more generally, introduced stronger local effects.

To investigate the mechanism behind the strut-induced effect, measurement planes $Y3$ and $Y4$ were positioned at the location of the second strut. While the flow fields are not resolved close enough to the surface to investigate this mechanism using PIV, CFD results do provide sufficient resolution. As shown in App. B in Fig. B2, the struts indeed appear to affect the local spanwise flow, evidenced by localized regions of increased and decreased u_y values, indicative of a strut-induced velocity increase. This

https://doi.org/10.5194/wes-2025-217
Preprint. Discussion started: 30 October 2025

eawe european academy of wind energy
Open Access WIND ENERGY SCIENCE DISCUSSIONS

interaction does not produce a uniform effect along the streamwise direction but develops progressively, particularly within the recirculation zone aft of the leading-edge tube.

To investigate this effect, four spanwise slices focused on the second strut, spanning from $x/c = 0.1$ to 0.3, are shown in Fig. 9. The first row displays the streamwise velocity u, where regions of increased upstream flow around the strut are indicated by blue contours. This corresponds to an increase in downward velocity u_z, also shown in blue in the second row, and enhanced spanwise velocity u_y, shown in red in the third row. Similar to the u component, the velocity differences in u_y and u_z become less pronounced downstream, as evident in the last column. The combination of increased downward, sideways, and upstream flow near the strut suggests the presence of a tilted or angled vortex structure.

To investigate whether vortices are present, the λ_2 criterion is plotted in the last row. It is derived from the eigenvalues of the symmetric tensor $\mathbf{E}^2 + \mathbf{W}^2$, where the square denotes a matrix multiplication yielding another second-order tensor. The symmetric strain rate and antisymmetric spin tensors are defined as

$$\mathbf{E} = \frac{1}{2}\left(\nabla\mathbf{u} + (\nabla\mathbf{u})^\mathsf{T}\right), \quad \text{and} \tag{10}$$

$$\mathbf{W} = \frac{1}{2}\left(\nabla\mathbf{u} - (\nabla\mathbf{u})^\mathsf{T}\right), \tag{11}$$

respectively, where $\nabla\mathbf{u}$ denotes the velocity gradient tensor.

The λ_2 criterion specifically evaluates the second-largest eigenvalue of this tensor, where $\lambda_2 < 0$ indicates the presence of a vortex core (Jeong and Hussain, 1995). The values reported here differ in magnitude from those in Viré et al. (2022) due to the adjustment in angle of attack, scaling to the projected frontal area rather than the projected side area, and the omission of the sign inversion applied in that study.

At $x/c = 0.1$, the λ_2-criterion indicates negative regions within the shear layer and close to the surface on the outward side of the strut. The latter region somewhat corresponds to areas of elevated u_y and u_z velocities. Closer to the strut, the shear layer structures begin to break down. The breaking down phenomenon intensifies downstream and coincides with a shear layer bump best observed in the u velocity plot, attributed to negative u_y regions. Another factor contributing to the breakdown of a well moving downstream is increased turbulent mixing. By $x/c = 0.3$, a region of negative λ_2 values has grown in size and now covers nearly the entire recirculation region.

In summary, the strut induces a local increase in flow velocity in all three spatial directions, indicating a strong 3D interaction. This effect cannot be attributed solely to spanwise 2D flow components, as elevated upstream velocities in the u direction were also observed within the strut region. These features suggest the presence of a 3D mechanism, such as an angled vortex originating near the inward tip side, that may account for the observed upstream flow. Although the upstream shear layer is clearly defined in the λ_2 plot, the existence of such a vortex could not be definitively confirmed. Nevertheless, the strut's influence on both velocity and vorticity shedding is apparent. Given the spatial overlap between these disturbed flow regions and planes $Y3$ and $Y4$, the strut effect is a credible contributor to the elevated lift and drag observed in the surface pressure integration. While global aerodynamic coefficients remain largely unaffected by strut inclusion, as reported by (Viré et al., 2022), this analysis demonstrates how the struts affect local aerodynamic phenomena, highlighting important implications for both experimental interpretation and sectional load modeling.

https://doi.org/10.5194/wes-2025-217
Preprint. Discussion started: 30 October 2025

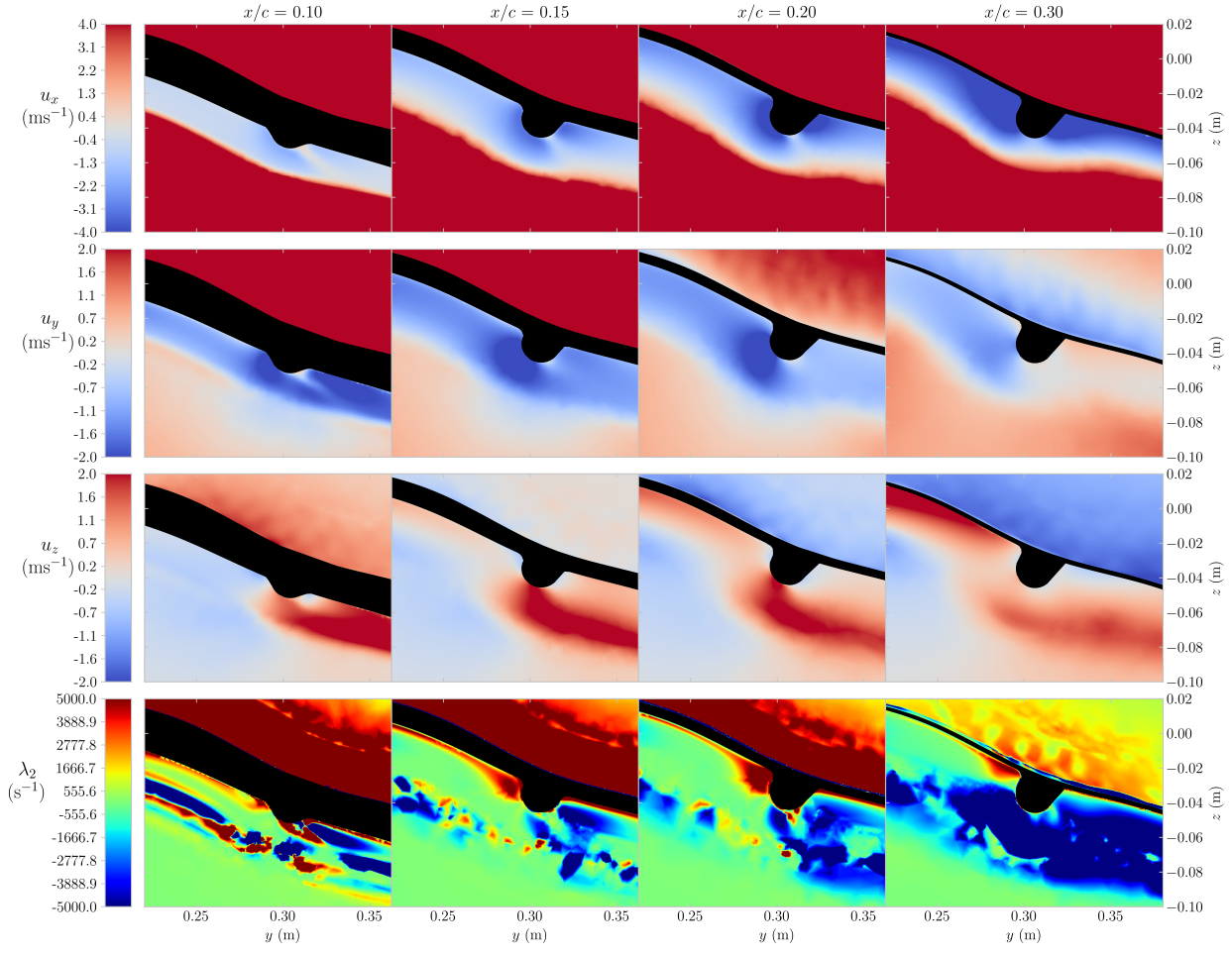

Figure 9. Spanwise CFD slices were generated at α = 7° and a Re $= 10 \times 10^5$. The columns show different x/c locations, indicating the development of the recirculation zone flow near the strut. The first columns intersect part of the leading-edge tube and fillet, and therefore do not capture the thin membrane, which becomes visible in the final column. The rows indicate the three flow velocity components u_x, u_y, and u_z, and the last row shows the λ_2-criterion.

https://doi.org/10.5194/wes-2025-217
Preprint. Discussion started: 30 October 2025

eawe european academy of wind energy
Open Access WIND ENERGY SCIENCE DISCUSSIONS

5 Conclusion

A novel stereoscopic particle image velocimetry (PIV) campaign was conducted in the Open-Jet Facility at TU Delft on a rigid 1:6.5 scale model of the TU Delft V3 leading-edge inflatable (LEI) kite. The addition of this experimentally measured flow-field dataset reinforces the model's status as a benchmark configuration for LEI kites. The experiments used the same idealized geometry with fillets as employed in simulations to ensure consistency in comparison.

The complex LEI wing geometry, including its double-curved anhedral canopy, near-cylindrical leading edge, and struts, includes surfaces that often face directly toward the laser light sheet, making them particularly prone to unwanted reflections. As a result, the authors hypothesize that reflections were the dominant source of anomalous velocity vectors in the PIV images. Despite the use of matte coatings, masked regions, and tailored processing, these effects remained significant, highlighting the need for further refinement of reflection suppression techniques for LEI wings.

Qualitatively, the PIV vector maps reproduce the principal flow-field features predicted by computational fluid dynamics (CFD), with velocity fields showing consistent magnitudes, particularly at an angle of attack of 17° in the wake and separated flow regions that are minimally affected by surface reflections. The location of stall onset, previously inferred only from three-dimensional (3D) integral load trends, was thus directly confirmed in the measurements, reinforcing the reliability of both methods in capturing key flow phenomena at high angles of attack.

Although surface-adjacent flow could not be fully resolved and some anomalous regions remained, quantitative comparison based on bound-curve integration remained feasible. Spanwise circulation extracted from the PIV measurements aligns well with both CFD and vortex step method predictions. Furthermore, loads derived from two-dimensional momentum integration of the measurements show good agreement with CFD, particularly when elliptical integration boundaries are applied at mid-span, where uncertainty was lowest.

Beyond validation, the numerical CFD analysis further indicates that the strut accelerates the local flow both spanwise and upstream, enlarging the downstream recirculation zone and redistributing shear-layer vorticity. This highlights the role of strut aerodynamics as a non-negligible factor in sectional load modeling and future kite wing planform optimization.

Future efforts are strongly encouraged to explore more effective methods for minimizing reflections, such as advanced coating solutions with ultra-low reflectivity. Implementing a volumetric measurement approach could enable the capture of more 3D effects, including strut-induced interactions. Additional insight may also be gained by analyzing the wake region, particularly the dynamics of tip vortices. Measurement quality could be further improved by employing a narrower laser light sheet to concentrate laser power, potentially reducing reflection intensity.

Code and data availability. The processed PIV measurements are available on Zenodo from https://doi.org/10.5281/zenodo.17395913. The code for the analysis of this data and the generation of the tables and diagrams in this paper is available on Zenodo from https://doi.org/10.5281/zenodo.17396075 and GitHub from https://github.com/jellepoland/kite_piv_analysis. The CFD data, presented in Viré et al. (2022), and used throughout this study is also available on Zenodo from https://doi.org/10.5281/zenodo.17395314. This code also includes vortex-step method (VSM) simulations, which were performed in the context of this study. The latest version of the VSM can be found

https://doi.org/10.5194/wes-2025-217
Preprint. Discussion started: 30 October 2025

on: https://github.com/awegroup/Vortex-Step-Method. The geometric mesh of the TU Delft V3 kite is available on Zenodo from https://doi.org/10.5281/zenodo.15316036 and GitHub from https://github.com/awegroup/TUDELFT_V3_LEI_KITE. More information on the TU Delft V3 Kite is available from https://awegroup.github.io/TUDELFT_V3_KITE/.

Author contributions. JAWP wrote the manuscript, co-designed the experiment, executed the experiment, and performed the analysis. EF co-designed the experiment, executed the experiment, aided in performing the analysis, and made several other contributions to the manuscript. RS supervised the project and made several contributions to the manuscript.

Competing interests. At least one of the (co-)authors is a member of the editorial board of Wind Energy Science.

Acknowledgements. The authors would like to thank the following people for their help: Mark van Spronsen for aiding in data gathering and co-designing the experiment. David Bensason for setting up the PIV and Frits Donker Duyvis for aiding with the laser and more. Mac Gaunaa, Andrea Sciacchitano, and Delphine de Tavernier for advice and guidance.

Financial support. This research has been supported by the Nederlandse Organisatie voor Wetenschappelijk Onderzoek (NWO) under grant number 17628. This work has partially been supported by the MERIDIONAL project, which receives funding from the European Union's 410 Horizon Europe Programme under the grant agreement No. 101084216. We acknowledge the use of OpenAI's ChatGPT and Grammarly for assistance in refining the writing style of this manuscript.

Appendix A: Noca's method, in reduced form

Noca et al. (1999) presented a 3D method for the computation of forces from a boundary surface, given sufficient flow-field information. In the present work, this method was applied under the assumption of 2D incompressible flow. To reduce the dimensions $\mathcal{N}$ from three to two, a zero was substituted in the second component of the normal vector,

$$\mathbf{n} = \begin{bmatrix} n_x & 0 & n_z \end{bmatrix}^\top, \tag{A1}$$

the position vector,

$$\mathbf{x} = \begin{bmatrix} x & 0 & z \end{bmatrix}^\top, \tag{A2}$$

and the velocity vector,

$$\mathbf{u} = \begin{bmatrix} u_x & 0 & u_z \end{bmatrix}^\top, \tag{A3}$$

https://doi.org/10.5194/wes-2025-217
Preprint. Discussion started: 30 October 2025

eawe european academy of wind energy
Open Access WIND ENERGY SCIENCE DISCUSSIONS

and the first and last components of the vorticity vector,

$$\boldsymbol{\omega} = \begin{bmatrix} 0 & \omega_y & 0 \end{bmatrix}^\top. \tag{A4}$$

As shown in Sect. 2.7, the second and third terms of Noca's equation, Eq. (5), fall away: the second term, representing momentum flux through the solid, impermeable surface, is zero due to the no-throughflow condition, and the third term, accounting for boundary acceleration, is zero since the body was stationary. In addition, the steady-flow assumption renders the time-derivative terms in the flux equation, corresponding to the second line of Eq. (6), equal to zero.

To derive the reduced form, the expressions were rewritten in matrix notation. A direct transfer of the symbolic ordering was not possible, since the left-hand side required a column vector, whereas the right-hand side produced a row vector. This inconsistency was resolved by reordering the dot product, placing the flux term before the surface normal,

$$\frac{\mathbf{F}}{\rho} = \oint_S \boldsymbol{\gamma}_{\text{flux}} \mathbf{n} \mathrm{d}s. \tag{A5}$$

Such a reordering is permissible without modification for symmetric dyadics, but non-symmetric dyadics, present at the third, fourth, and ninth terms, had to be explicitly rewritten by taking the transpose.

A1 Inviscid terms

The first four terms are the inviscid contributions. The first was reduced to

$$\frac{1}{2}\oint_S (u^2\mathbf{I})\mathbf{n}\mathrm{d}s = \frac{1}{2}\oint_S \left((u_x^2+u_z^2) \begin{bmatrix} 1 & 0 & 0 \\ 0 & 1 & 0 \\ 0 & 0 & 1 \end{bmatrix} \right) \begin{bmatrix} n_x \\ 0 \\ n_z \end{bmatrix} \mathrm{d}s = \frac{1}{2}\oint_S \begin{bmatrix} n_x(u_x^2+u_z^2) \\ 0 \\ n_z(u_x^2+u_z^2) \end{bmatrix} \mathrm{d}s, \tag{A6}$$

the second to

$$-\oint_S (\mathbf{u}\mathbf{u}^\top)\mathbf{n}\mathrm{d}s = -\oint_S \left(\begin{bmatrix} u_x \\ 0 \\ u_z \end{bmatrix} \begin{bmatrix} u_x & 0 & u_z \end{bmatrix} \right) \begin{bmatrix} n_x \\ 0 \\ n_z \end{bmatrix} \mathrm{d}s = -\oint_S \begin{bmatrix} n_x u_x^2 + n_z u_z u_x \\ 0 \\ n_x u_x u_z + n_z u_z^2 \end{bmatrix} \mathrm{d}s, \tag{A7}$$

the third to

$$-\frac{1}{\mathscr{N}-1}\oint_S \left[(\mathbf{x}\times\boldsymbol{\omega})\mathbf{u}^\top\right]\mathbf{n}\mathrm{d}s = -\oint_S \left(\begin{bmatrix} -z\omega_y \\ 0 \\ x\omega_y \end{bmatrix} \begin{bmatrix} u_x & 0 & u_z \end{bmatrix} \right) \begin{bmatrix} n_x \\ 0 \\ n_z \end{bmatrix} \mathrm{d}s = \oint_S \begin{bmatrix} (n_x u_x + n_z u_z) z\omega_y \\ 0 \\ -(n_x u_x + n_z u_z) x\omega_y \end{bmatrix} \mathrm{d}s. \tag{A8}$$

and the fourth to

$$\frac{1}{\mathscr{N}-1}\oint_S \left[(\mathbf{x}\times\mathbf{u})\boldsymbol{\omega}^\top\right]\mathbf{n}\mathrm{d}s = \oint_S \left(\begin{bmatrix} 0 \\ xu_z - zu_x \\ 0 \end{bmatrix} \begin{bmatrix} 0 & \omega_z & 0 \end{bmatrix} \right) \begin{bmatrix} n_x \\ 0 \\ n_z \end{bmatrix} \mathrm{d}s = \begin{bmatrix} 0 \\ 0 \\ 0 \end{bmatrix}. \tag{A9}$$

https://doi.org/10.5194/wes-2025-217
Preprint. Discussion started: 30 October 2025

eawe european academy of wind energy
Open Access WIND ENERGY SCIENCE DISCUSSIONS

A2 Viscous terms

The last line of Eq. (6) contains the viscous terms, where the viscous stress tensor $\boldsymbol{\tau}$ appears. Defined in Cartesian coordinates, it was reduced to

$$\boldsymbol{\tau} = \mu \begin{bmatrix} 2\frac{\partial u_x}{\partial x} - \frac{2}{3}(\nabla\cdot\mathbf{u}) & \frac{\partial u_x}{\partial y} + \frac{\partial u_y}{\partial x} & \frac{\partial u_x}{\partial z} + \frac{\partial u_z}{\partial x} \\ \frac{\partial u_y}{\partial x} + \frac{\partial u_x}{\partial y} & 2\frac{\partial u_y}{\partial y} - \frac{2}{3}(\nabla\cdot\mathbf{u}) & \frac{\partial u_y}{\partial z} + \frac{\partial u_z}{\partial y} \\ \frac{\partial u_z}{\partial x} + \frac{\partial u_x}{\partial z} & \frac{\partial u_z}{\partial y} + \frac{\partial u_y}{\partial z} & 2\frac{\partial u_z}{\partial z} - \frac{2}{3}(\nabla\cdot\mathbf{u}) \end{bmatrix} = \mu \begin{bmatrix} 2\frac{\partial u_x}{\partial x} & 0 & \frac{\partial u_x}{\partial z} + \frac{\partial u_z}{\partial x} \\ 0 & 0 & 0 \\ \frac{\partial u_z}{\partial x} + \frac{\partial u_x}{\partial z} & 0 & 2\frac{\partial u_z}{\partial z} \end{bmatrix}, \tag{A10}$$

and its divergence becomes

$$\nabla\boldsymbol{\tau} = \mu \begin{bmatrix} 2\frac{\partial^2 u_x}{\partial x^2} + \frac{\partial^2 u_z}{\partial x \partial z} + \frac{\partial^2 u_x}{\partial z^2} \\ 0 \\ \frac{\partial^2 u_x}{\partial x \partial z} + \frac{\partial^2 u_z}{\partial x^2} + 2\frac{\partial^2 u_z}{\partial z^2} \end{bmatrix} = \mu \begin{bmatrix} \Pi_1 \\ 0 \\ \Pi_3 \end{bmatrix}. \tag{A11}$$

Substituting the reduced forms into the eighth term gives

$$\frac{1}{\mathcal{N}-1} \oint_S \left[\left(\mathbf{x}^\mathsf{T}(\nabla\boldsymbol{\tau})\right)\mathbf{I} \right] \mathbf{n} \mathrm{d}s = \mu \oint_S \left(\begin{bmatrix} x & 0 & z \end{bmatrix} \begin{bmatrix} \Pi_1 \\ 0 \\ \Pi_3 \end{bmatrix} \right) \mathbf{I} \begin{bmatrix} n_x \\ 0 \\ n_z \end{bmatrix} \mathrm{d}s = \mu \oint_S \begin{bmatrix} n_x(x\Pi_1 + z\Pi_3) \\ 0 \\ n_z(x\Pi_1 + z\Pi_3) \end{bmatrix} \mathrm{d}s. \tag{A12}$$

The ninth term is reduced to

$$-\frac{1}{\mathcal{N}-1} \oint_S \left[(\nabla\boldsymbol{\tau})\mathbf{x}^\mathsf{T} \right] \mathbf{n} \mathrm{d}s = -\mu \oint_S \left(\begin{bmatrix} \Pi_1 \\ 0 \\ \Pi_3 \end{bmatrix} \begin{bmatrix} x & 0 & z \end{bmatrix} \right) \begin{bmatrix} n_x \\ 0 \\ n_z \end{bmatrix} \mathrm{d}s = -\mu \oint_S \begin{bmatrix} \Pi_1(xn_x + zn_z) \\ 0 \\ \Pi_3(xn_x + zn_z) \end{bmatrix} \mathrm{d}s. \tag{A13}$$

Finally, the tenth term became

$$\oint_S \boldsymbol{\tau}\mathbf{n} \mathrm{d}s = \mu \oint_S \begin{bmatrix} 2\frac{\partial u_x}{\partial x} & 0 & \frac{\partial u_x}{\partial z} + \frac{\partial u_z}{\partial x} \\ 0 & 0 & 0 \\ \frac{\partial u_z}{\partial x} + \frac{\partial u_x}{\partial z} & 0 & 2\frac{\partial u_z}{\partial z} \end{bmatrix} \begin{bmatrix} n_x \\ 0 \\ n_z \end{bmatrix} \mathrm{d}s = \mu \oint_S \begin{bmatrix} n_x\left(2\frac{\partial u_x}{\partial x}\right) + n_z\left(\frac{\partial u_x}{\partial z} + \frac{\partial u_z}{\partial x}\right) \\ 0 \\ n_x\left(\frac{\partial u_z}{\partial x} + \frac{\partial u_x}{\partial z}\right) + n_z\left(2\frac{\partial u_z}{\partial z}\right) \end{bmatrix} \mathrm{d}s. \tag{A14}$$

https://doi.org/10.5194/wes-2025-217
Preprint. Discussion started: 30 October 2025

eawe european academy of wind energy
Open Access WIND ENERGY SCIENCE DISCUSSIONS

A3 Reduced form

Combining everything, the following reduced form was obtained:

$$\frac{F_x}{\rho} = \oint_S \left[\frac{1}{2} n_x \left(u_z^2 - u_x^2\right) - n_z u_x u_z + (n_x u_x + n_z u_z) z\omega_y + \mu n_x (x\Pi_1 + z\Pi_3) - \mu \Pi_1 (x n_x + z n_z) \right.$$
$$\left. + \mu \left(2n_x \frac{\partial u_x}{\partial x} + n_z \left(\frac{\partial u_x}{\partial z} + \frac{\partial u_z}{\partial x} \right) \right) \right] \mathrm{d}s,$$
$$\frac{F_z}{\rho} = \oint_S \left[\frac{1}{2} n_z \left(u_x^2 - u_z^2\right) - n_x u_x u_z - (n_x u_x + n_z u_z) x\omega_y + \mu n_z (x\Pi_1 + z\Pi_3) - \mu \Pi_3 (x n_x + z n_z) \right.$$
$$\left. + \mu \left(n_x \left(\frac{\partial u_x}{\partial z} + \frac{\partial u_z}{\partial x} \right) + 2n_z \frac{\partial u_z}{\partial z} \right) \right] \mathrm{d}s, \tag{A15}$$

with

$$\Pi_1 = 2\frac{\partial^2 u_x}{\partial x^2} + \frac{\partial^2 u_z}{\partial x \partial z} + \frac{\partial^2 u_x}{\partial z^2}, \qquad \Pi_3 = \frac{\partial^2 u_x}{\partial x \partial z} + \frac{\partial^2 u_z}{\partial x^2} + 2\frac{\partial^2 u_z}{\partial z^2}. \tag{A16}$$

Appendix B: Masking

The three velocity components u_x, u_y and u_z of plane $Y1$, unmasked and masked are shown in Fig. B1. The raw u_y-component plot reveals areas with unrealistically high out-of-plane velocities that are not expected in the symmetry plane of the wing. The color bar is limited to ± 3 ms^{-1} for better interpretability. The u_x and u_y velocity components in the same areas also exhibit unrealistic values. Comparisons with raw images revealed that reflections in these areas prohibited accurate PIV processing. This led to the conclusion that the discussed regions require a masking procedure.

Using the standard deviation as a mask to remove these regions proved ineffective because it could not capture all the zones and removed many data points outside the identified regions. This was especially prevalent in the α = 17° case, where a large separated flow region is present that, given its unsteady nature, fluctuates substantially over the 250 images, thereby causing large standard deviations that would have consequently been filtered out. The lateral velocity component u_y provided the best proxy to filter out the data points, which also removed most of the off-predicted u_x and u_z regions due to the overlap with the off-predicted u_y regions.

Both the identification of regions as off-prediction and selecting $\pm$ 3 ms^{-1} u_y to mask the experimental data were motivated by comparing the measured data to numerical data. Two spanwise slices are plotted in Fig. B2, which show that no u_y components outside of $\pm$ 3 ms^{-1} range are present for the measurement planes, except the $Y7$ plane for the α = 6° case. With α = 17°, a larger white region shows but does not cross any of the measurement planes, i.e., at this α, only up to $Y4$ located at $y = 0.301$ m, measured were made.

https://doi.org/10.5194/wes-2025-217
Preprint. Discussion started: 30 October 2025

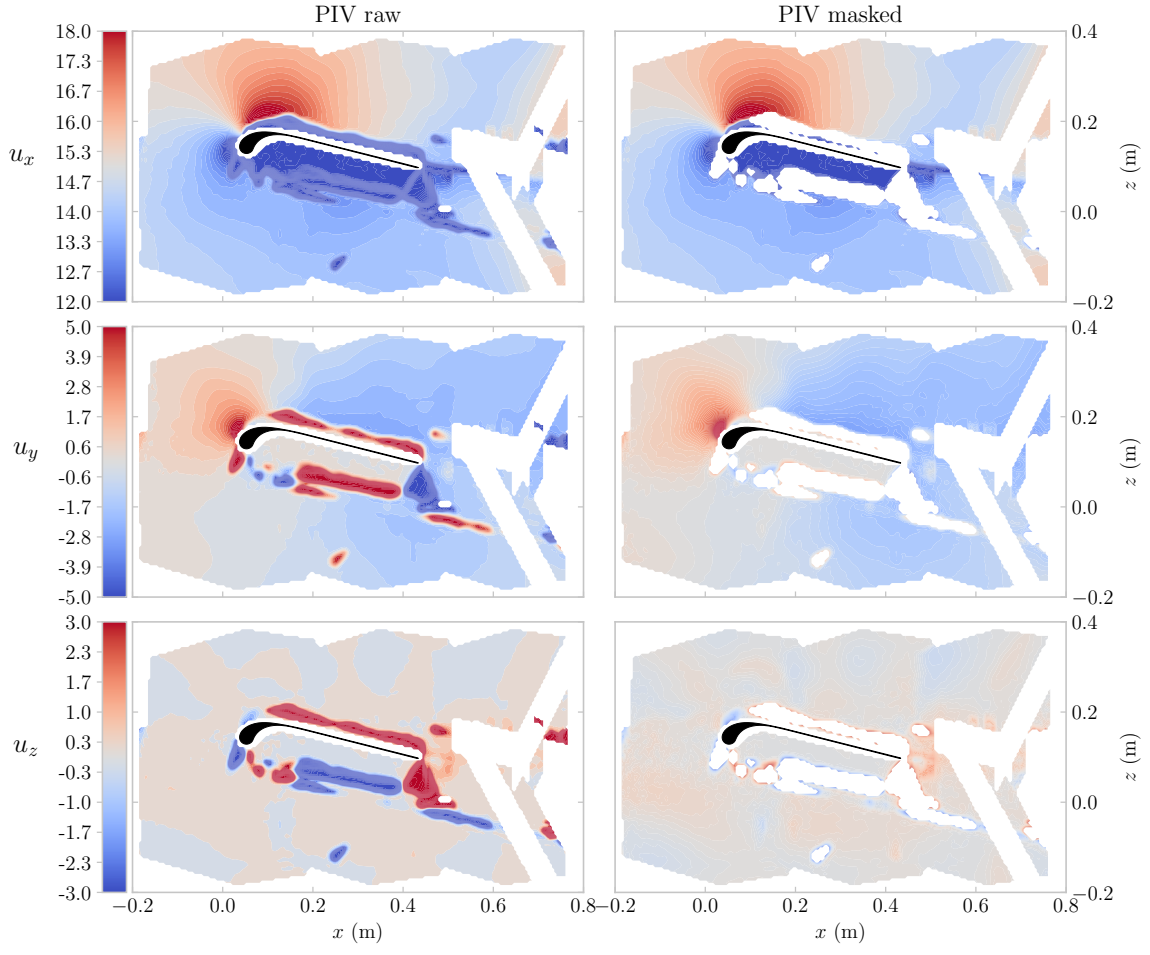

Figure B1. The first column indicates the unmasked raw PIV images for the three velocity components u_x, u_y and u_z at measurement plane $Y1$ and α is 6°. The second column shows the same plane, but masked using a u_z filter.

https://doi.org/10.5194/wes-2025-217
Preprint. Discussion started: 30 October 2025

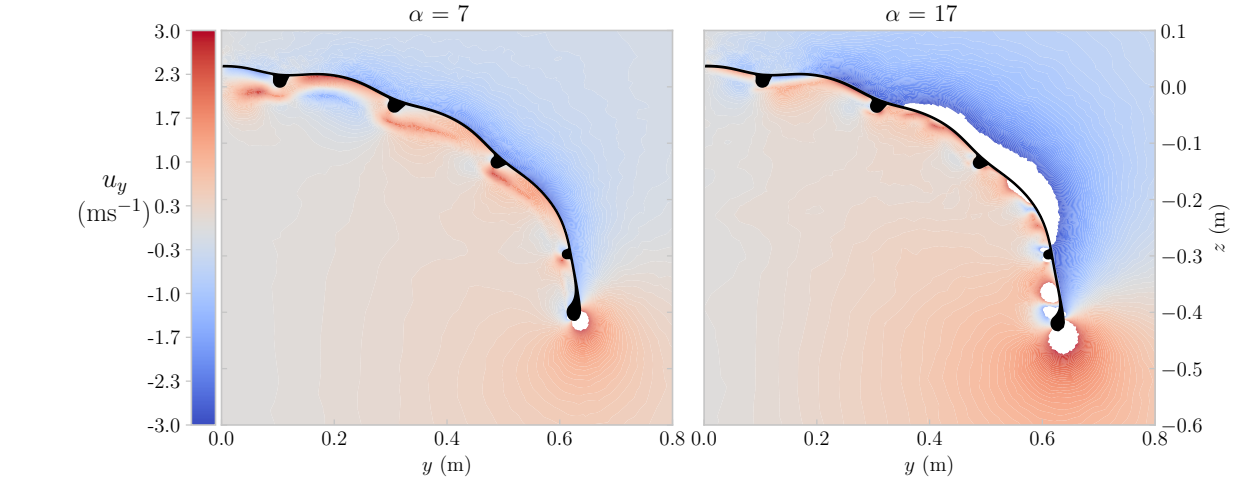

Figure B2. Spanwise slices of the u_y flow fields made using the data from Viré et al. (2022), the left showing the $\alpha = 7°$ case and the right the 17° case. The white regions indicate where the absolute u_y velocity is larger than 3 ms^{-1}. The displayed slices are taken at 0.25 x/c offset from the leading edge in the stream-wise x direction.

Appendix C: Defining boundary curves

To obtain aerodynamic properties of a flow field, the methods described in Sect. 2.7 are used and require a boundary curve. Two curve shapes were used, an ellipse and a rectangle, illustrated for both CFD and PIV at $Y2$ and $Y5$ with α is 7° in Fig. C1. The boundary curves are described by a number of nodes N_b. For each boundary node $N_{\mathrm{b,i}}$, the flow field data inside a square of 0.05 m by 0.05 m centered at $N_{\mathrm{b,i}}$ was interpolated to populate $N_{\mathrm{b,i}}$.

When analyzing the PIV-measurement planes, certain boundary curves cross regions without flow field data. Each encountered empty flow field node inside an interpolation square is populated by an additional interpolation using the neighboring nodes. Examples of interpolation squares crossing initially empty flow fields are indicated by the black squares in the second column of Fig. C1.

The boundary curves are defined by an x center coordinate x_b, a z center coordinate z_b, rotation angle, width W_b, height H_b, and N_b. The center locations are set equal to the airfoil centroids. To determine suitable W_b and H_b values, a convergence study was done on the lift calculated with Noca's method $C_{\mathrm{l,\,Noca}}$ and the circulation Γ.

https://doi.org/10.5194/wes-2025-217
Preprint. Discussion started: 30 October 2025

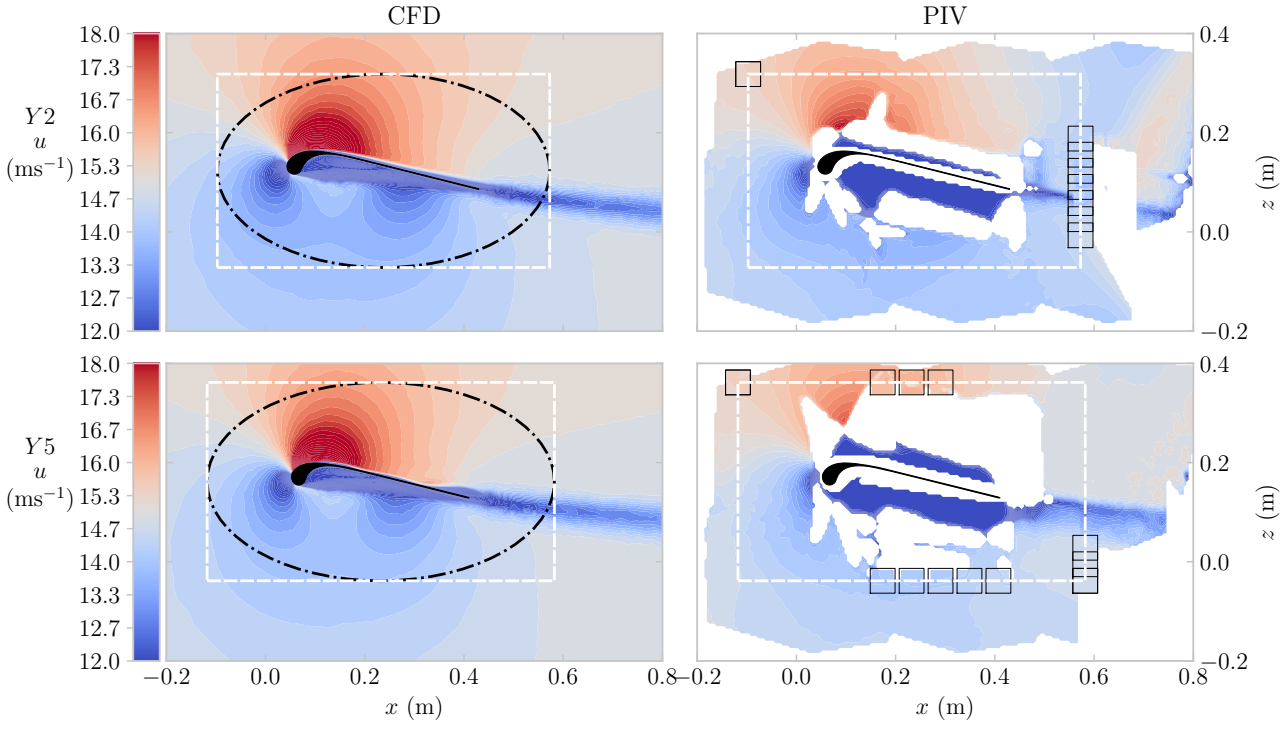

Figure C1. The left column shows CFD and the right column PIV, both colored by the velocity magnitude u. The top row contains the $Y2$ plane and the bottom the $Y5$ plane, both measured at $\alpha = 7°$. The white rectangle and the black ellipse represent the two investigated boundary shapes, and the smaller black squares in the right column represent the PIV locations for which additional interpolation was required to ensure sufficient data presence for populating the boundary nodes.

The sensitivity results are shown for $Y2$ with $\alpha = 6°$ in Fig C2. The first column shows the variation when only changing N_b, where both CFD and PIV results show a converging trend for $C_{\mathrm{l,\,Noca}}$ and Γ. For PIV, the rectangle shape predicts different values. In the second and third columns, the boundary width W_b and height H_b are plotted, and the individual data points are plotted with a color to indicate the % of interpolated data points; where data points that required more than 1% of interpolation are filtered out. The CFD results exhibit good convergence for both variations in W_b and H_b. Both the ellipse and rectangle shapes show close agreement in the values of $C_{\mathrm{l,\,Noca}}$, with only a small deviation in the circulation, Γ. In contrast, the PIV results often fail to converge, with frequent misalignment between the ellipse and rectangle shape predictions.

The 'optimal' number of nodes was determined considering the convergence of circulation Γ and the drag predicted by the Noca's method $C_{\mathrm{d,\,Noca}}$. All planes converged when increasing N_b. A value of 360 nodes was selected for all planes. Determining the parameters W_b and H_b was done iteratively for each plane and α separately. The resulting curves were

https://doi.org/10.5194/wes-2025-217
Preprint. Discussion started: 30 October 2025

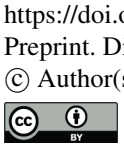

eawe european academy of wind energy
Open Access WIND ENERGY SCIENCE DISCUSSIONS

checked visually and numerically using the % of interpolated empty flow field points to ensure that the curve crossed as much as possible through the measured flow field. On top of that, the neighboring points, e.g., not only 0.4m wide but also 0.41m wide, were checked using the same criteria. A vertical line is present in all plots, indicating the selected values, which, together with the centers, are reported in Table 4 for all planes.

As the sensitivity analysis showed that the PIV flow field is sensitive to the boundary curve parameters, i.e., does not converge well, the analysis was done on a total of 100 combinations of W_b and H_b and averaged, to reduce inconsistencies. The 100 combinations comprise of 10 W_b values and 10 H_b values and span a $\pm$ 10% region, indicated in the plots by the vertical grey band, around the 'optimal' value. A sensitivity analysis was performed on the rotation angle and over a sweep of $\pm 10°$, less than 0.01 difference in $C_{\mathrm{l,\,Noca}}$ and Γ was seen, hence not reported here.

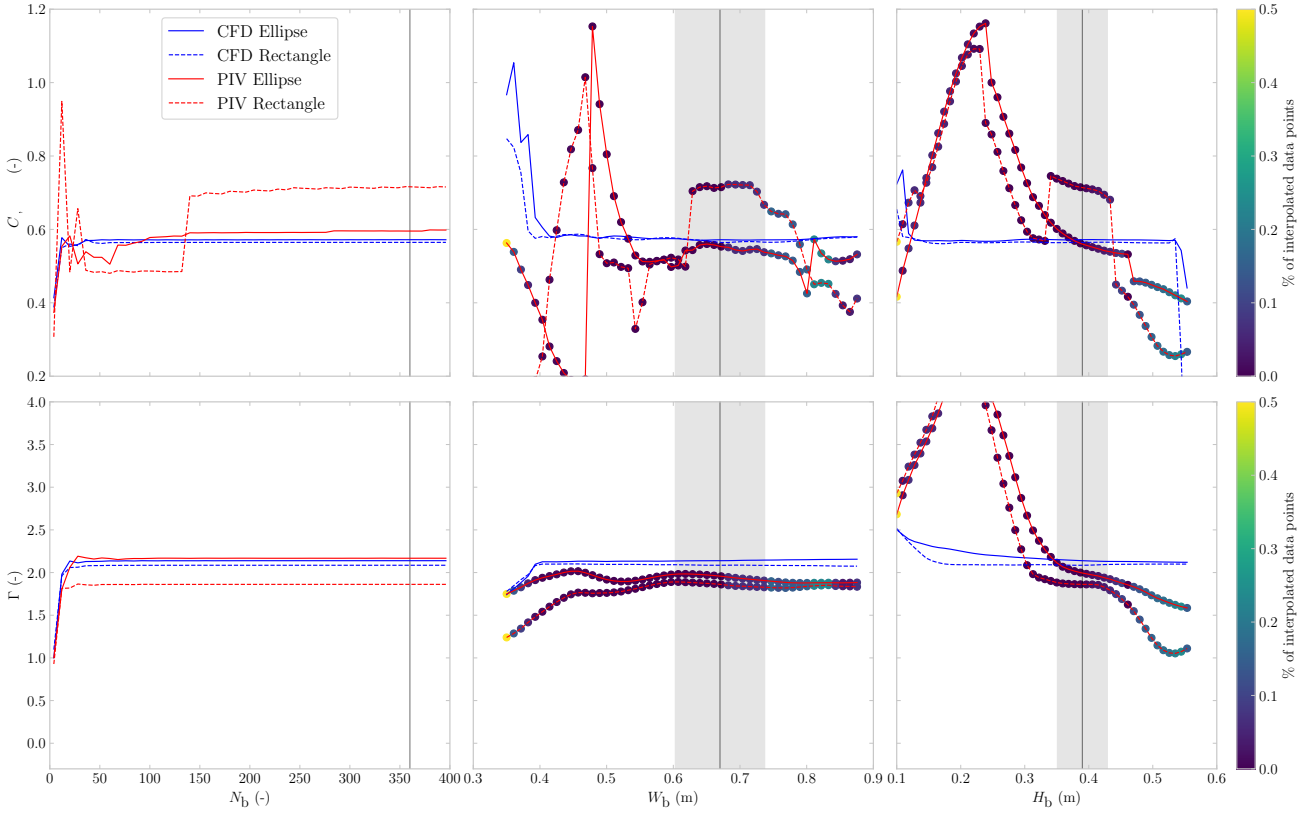

Figure C2. Convergence analysis for $Y2$ the boundary curve setting, i.e. N_b, W_b and H_b, used for calculation $C_{\mathrm{l,\,Noca}}$ presented in the top row and Γ reported in the bottom row. Each plot contains a vertical line, indicating the determined 'optimal' value, and the vertical grey band indicates the region that was used for averaging.

https://doi.org/10.5194/wes-2025-217
Preprint. Discussion started: 30 October 2025

eawe european academy of wind energy
Open Access WIND ENERGY SCIENCE DISCUSSIONS

Appendix D: Convergence over the 250 image samples

To test if the 250 images were sufficient to average the data, the mid-chord suction side measurement of $Y4$ at α = 17° was analyzed. This plane was chosen as it has the largest uncertainty, see Table 3, rendering it less likely to show good convergence, enabling a conservative estimate. To analyze the convergence, the u_x, u_y and u_z velocities of a specific point are plotted in Fig. D1. To do so, the 250 analyzed images were randomly shuffled; hence, one can not infer anything from the local value pattern. In the local coordinates of the image the point is located at $x = -0.75\text{mm}$ and $z = -118.18\text{mm}$, which corresponds to roughly 0.25 m in both x and z in the reference frame used in this paper, e.g. as shown in Fig. 6. This analysis confirms that even at this challenging location, the PIV-processed velocity field averaged over 250 images is well-converged.

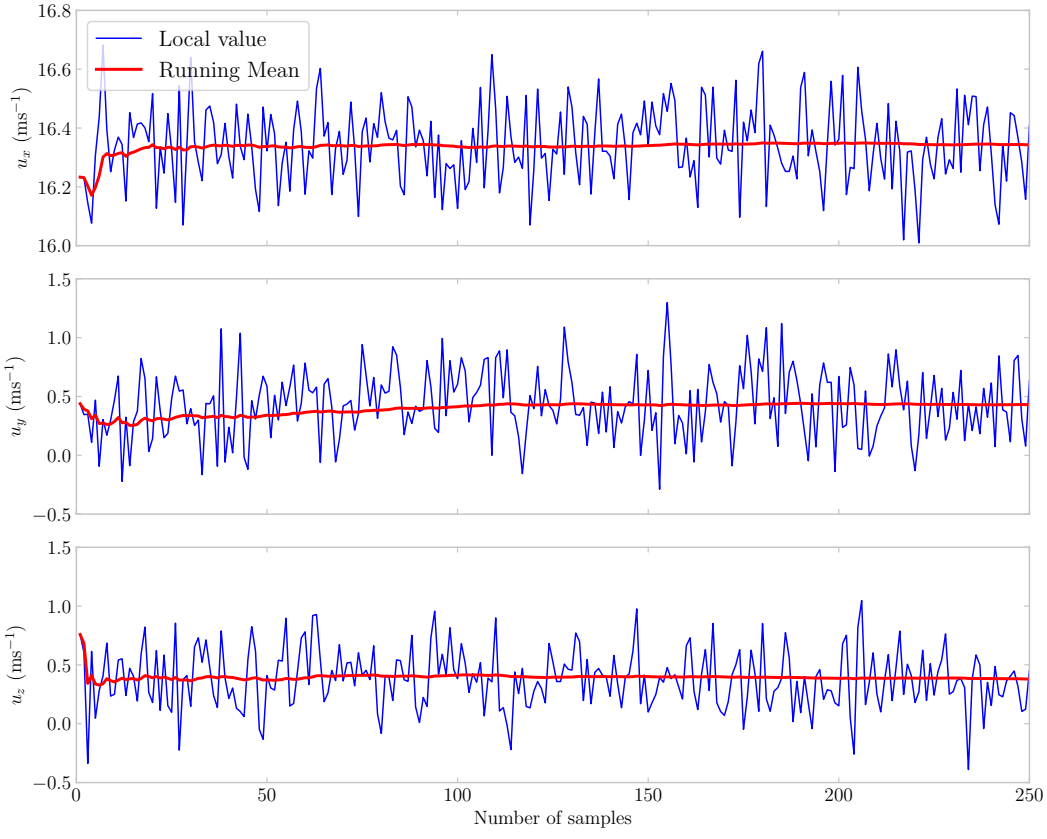

Figure D1. Randomly shuffled u_x, u_y, and u_z velocities of a point above the surface of the airfoil of plane $Y4$ at $\alpha = 17°$.

https://doi.org/10.5194/wes-2025-217
Preprint. Discussion started: 30 October 2025

eawe european academy of wind energy
Open Access WIND ENERGY SCIENCE DISCUSSIONS

References

Anderson, J. D.: Fundamentals of aerodynamics, McGraw-Hill Inc., 5th edn., ISBN 9780073398105, 2016.

Belloc, H.: Wind Tunnel Investigation of a Rigid Paraglider Reference Wing, Journal of Aircraft, 52, 703–708, https://doi.org/https://doi.org/10.2514/1.C032513, 2015.

Bensason, D., Sciacchitano, A., and Ferreira, C.: On the wake re-energization of the X-Rotor vertical-axis wind turbine via the vortex-generator strategy, Wind Energy Science Discussions, 2025, 1–37, https://doi.org/10.5194/wes-2025-3, 2025.

Breukels, J.: An Engineering Methodology for Kite Design, Ph.D. thesis, Delft University of Technology, Delft, http://resolver.tudelft.nl/uuid:cdece38a-1f13-47cc-b277-ed64fdda7cdf, 2011.

Cayon, O., Gaunaa, M., and Schmehl, R.: Fast Aero-Structural Model of a Leading-Edge Inflatable Kite, Energies, 16, 3061, https://doi.org/10.3390/en16073061, 2023.

Cayon, O., Watson, S., and Schmehl, R.: Kite as a Sensor: Wind and State Estimation in Tethered Flying Systems, Wind Energy Science Discussions, https://doi.org/10.5194/wes-2024-182, 2025.

Damiani, R., Wendt, F., Jonkman, J., and Sicard, J.: A Vortex Step Method for Nonlinear Airfoil Polar Data as Implemented in KiteAeroDyn, in: Proceedings of the AIAA Scitech 2019 Forum, San Diego, CA, USA, https://doi.org/10.2514/6.2019-0804, 2019.

De Wachter, A.: Deformation and Aerodynamic Performance of a Ram-Air Wing, Master's thesis, Delft University of Technology, https://resolver.tudelft.nl/uuid:786e3395-4590-4755-829f-51283a8df3d2, 2008.

Desai, S., Schetz, J. A., Kapania, R. K., and Gupta, R.: Wind Tunnel Testing of Tethered Inflatable Wings, Journal of Aircraft, 0, 1–18, https://doi.org/10.2514/1.C037437, 2024.

Elfert, C., Göhlich, D., and Schmehl, R.: Measurement of the turning behaviour of tethered membrane wings using automated flight manoeuvres, Wind Energy Science, 9, 2261–2282, https://doi.org/10.5194/wes-9-2261-2024, 2024.

Folkersma, M., Schmehl, R., and Viré, A.: Flow transition modeling on two-dimensional circular leading edge airfoils, Wind Energy, 22, 908–921, https://doi.org/10.1002/we.2329, 2019.

Fritz, E., Boorsma, K., and Ferreira, C.: Experimental analysis of a horizontal-axis wind turbine with swept blades using PIV data, Wind Energy Science, 9, 1617–1629, https://doi.org/10.5194/wes-9-1617-2024, 2024a.

Fritz, E., Ribeiro, A., Boorsma, K., and Ferreira, C.: Aerodynamic characterisation of a thrust-scaled IEA 15 MW wind turbine model: experimental insights using PIV data, Wind Energy Science, 9, 1173–1187, https://doi.org/10.5194/wes-9-1173-2024, 2024b.

Gaunaa, M. et al.: A Computationally Efficient Method for Determining the Aerodynamic Performance of Kites for Wind Energy Applications, in: EWEA Annual Event 2011, European Wind Energy Association (EWEA), https://backend.orbit.dtu.dk/ws/portalfiles/portal/6241674/Gaunaa_poster_EWEA2011presentation%5B1%5D.pdf, 2011.

Huang, M., Sciacchitano, A., and Ferreira, C.: On the wake deflection of vertical axis wind turbines by pitched blades, Wind Energy, 26, 365–387, https://doi.org/10.1002/we.2803, 2023.

Hummel, J., Göhlich, D., and Schmehl, R.: Automatic measurement and characterization of the dynamic properties of tethered membrane wings, Wind Energy Science, 4, 41–55, https://doi.org/10.5194/wes-4-41-2019, 2019.

Jeong, J. and Hussain, F.: On the identification of a vortex, Journal of Fluid Mechanics, 285, 69–94, https://doi.org/10.1017/S0022112095000462, 1995.

LaVision GmbH: LaVision Imaging Solutions for Flow, Spray, Combustion, and Materials Testing, https://www.lavision.de/en/, 2025.

https://doi.org/10.5194/wes-2025-217
Preprint. Discussion started: 30 October 2025

Lebesque, G.: Steady-State RANS Simulation of a Leading Edge Inflatable Wing with Chordwise Struts, Master's thesis, Delft University of Technology, https://resolver.tudelft.nl/uuid:f0bc8a1e-088d-49c5-9b77-ebf9e31cf58b, 2020.

LeBlanc, B. and Ferreira, C.: Estimation of blade loads for a variable pitch vertical axis wind turbine from particle image velocimetry, Wind Energy, 25, 313–332, https://doi.org/10.1002/we.2674, 2022.

Leloup, R., Roncin, K., Bles, G., Leroux, J. B., Jochum, C., and Parlier, Y.: Estimation of the lift-to-drag ratio using the lifting line method: Application to a leading edge inflatable kite, in: Airborne Wind Energy, edited by Ahrens, U., Schmehl, R., and Diehl, M., chap. 19, pp. 339–355, Springer, https://doi.org/10.1007/978-3-642-39965-7_19, 2013.

Lignarolo, L., Ragni, D., Krishnaswami, C., Chen, Q., Ferreira, C. S., and van Bussel, G.: Experimental Analysis of the Wake of a Horizontal-Axis Wind-Turbine Model, Renewable Energy, 70, 31–46, https://doi.org/10.1016/j.renene.2014.01.020, 2014.

Liu, L. Q., Zhu, J. Y., and Wu, J. Z.: Lift and drag in two-dimensional steady viscous and compressible flow, Journal of Fluid Mechanics, 784, 304–341, https://doi.org/10.1017/jfm.2015.584, 2015.

Masure, K. R. G.: Regression Model of Leading Edge Inflatable Kite Profile Aerodynamics, Master's thesis, Delft University of Technology, https://resolver.tudelft.nl/uuid:865d59fc-ccff-462e-9bac-e81725f1c0c9, 2025.

Noca, F., Shiels, D., and Jeon, D.: A comparison of methods for evaluating time-dependant fluid dynamic forces on bodies, using only velocity fields and their derivatives, Journal of Fluids and Structures, 13, 551–578, https://doi.org/10.1006/jfls.1999.0219, 1999.

Oehler, J. and Schmehl, R.: Aerodynamic characterization of a soft kite by in situ flow measurement, Wind Energy Science, 4, 1–21, https://doi.org/10.5194/wes-4-1-2019, 2019.

Poland, J. A. W., Masure, K. R. G., Cayon, O., and Schmehl, R.: [in preparation] Aerodynamic simulations for kite design, Wind Energy Science, 2025a.

Poland, J. A. W., van Spronsen, J. M., Gaunaa, M., and Schmehl, R.: Wind Tunnel Load Measurements of a Leading-Edge Inflatable Kite Rigid Scale Model, Wind Energy Science, https://doi.org/https://doi.org/10.5194/wes-2025-77, [under review, preprint available], 2025b.

Prasad, A. K.: Stereoscopic particle image velocimetry, Experiments in Fluids, 29, 103–116, https://doi.org/10.1007/s003480000143, 2000.

Prasad, Ajay K. and Adrian, Ronald J.: Stereoscopic particle image velocimetry applied to liquid flows, Experiments in Fluids, 15, 49–60, https://doi.org/10.1007/BF00195595, 1993.

Raffel, M., Willert, C. E., Scarano, F., Kähler, C. J., Wereley, S. T., and Kompenhans, J.: Particle Image Velocimetry: A Practical Guide, Springer, Berlin, Germany, https://doi.org/10.1007/978-3-319-68852-7, 2018.

Sciacchitano, A. and Wieneke, B.: PIV uncertainty propagation, Measurement Science and Technology, 27, 084 006, https://doi.org/10.1088/0957-0233/27/8/084006, 2016.

Viré, A., Demkowicz, P., Folkersma, M., Roullier, A., and Schmehl, R.: Reynolds-averaged Navier-Stokes simulations of the flow past a leading edge inflatable wing for airborne wind energy applications, Journal of Physics: Conference Series, 1618, 032 007, https://doi.org/10.1088/1742-6596/1618/3/032007, 2020.

Viré, A., Lebesque, G., Folkersma, M., and Schmehl, R.: Effect of Chordwise Struts and Misaligned Flow on the Aerodynamic Performance of a Leading-Edge Inflatable Wing, Energies, 15, 1450, https://doi.org/10.3390/en15041450, 2022.

Watchorn, P.: Aerodynamic Load Modelling for Leading Edge Inflatable Kites, Master's thesis, Delft University of Technology, https://resolver.tudelft.nl/uuid:42f611a2-ef79-4540-a43c-0ea827700388, 2023.